Power-Aware Analog to Digital Converters

Satish Mulleti, Ayush Bhandari, and Yonina C. Eldar

1 Introduction

Almost all modern world systems rely on digital acquisition of the underlying continuous entities (e.g., Wi-Fi signals, temperatures, and audiovisual information among others). Not surprisingly, the digital acquisition protocol is critical to the data being captured through various modalities such as medical devices, smart-home sensors, autonomous vehicles, communication systems, and more. Typically, the data or signal is analog in nature, but different tasks that are performed on the data, such as extracting information, storing, or transmitting, can be more efficiently carried out in the digital domain. Signal processing algorithms implemented on digital signal processors are easier to control, less expensive, and more flexible than their analog counterparts. In addition, digital data is easier to store and transmit.

Sampling Theory acts as a bridge between the analog and the digital worlds. Specifically, sampling is a process of discrete representation of analog signals. There could be multiple discrete representations for a given analog signal depending on the application and the end goal. For example, the end goal could be a perfect reconstruction of the analog signal or estimating a few of its parameters from its discrete measurements. Hence, the discrete representation should capture the necessary information of the analog signal through the sampling mechanism. In

S. Mulleti (✉)
Indian Institute of Technology Bombay, Mumbai, India

A. Bhandari
Imperial College London, London, UK
e-mail: ayush@alum.mit.edu

Y. C. Eldar
Weizmann Institute of Science, Rehovot, Israel
e-mail: yonina.eldar@weizmann.ac.il

S. D. Casey et al. (eds.), *Sampling, Approximation, and Signal Analysis*, Applied and Numerical Harmonic Analysis, https://doi.org/10.1007/978-3-031-41130-4_16

practice, sampling is realized by an analog-to-digital converter (ADC) [1]. The process of an ADC is logically divided into two steps:

1. Sampling: mapping analog signals to a set of discrete-time, continuous-valued measurements, and
2. Quantization: the continuous-valued measurements are *digitized*—mapped to discrete-amplitudes—by assigning a finite number of bits to each measurement.

The analog signal can be perfectly recovered from the sampled measurements provided that there are a sufficient number of measurements. However, quantization is a lossy process, leading to distortion in the reconstruction. The architecture and working principles of ADCs depend on their digital representation. For example, the ADCs can be designed to measure instantaneous samples of the analog signal [1–4] or measure time instants when the analog signal crosses a certain threshold [5–14].

While designing systems such as handheld ultrasound scanners, miniature satellites, wireless sensors, and other compact devices, much importance is given to lower power consumption as these systems operate on a battery or a solar powered device. Such compact systems have a wider reach compared to their conventional counterparts. For example, a handheld ultrasound device can be used to diagnose patients in rural areas and underdeveloped regions where installing a conventional ultrasound device is not possible due to its high cost and power requirements [15, 16]. Since ADCs are an integral component of such systems, it is desirable to use a low-power ADC to reduce the cost and enable long-term operation. The power consumption of an ADC is closely tied to its architecture. The design parameters of an ADC, such as the sampling rate, dynamic range, and the number of quantization levels, dictate the power requirements. In addition, analog signals are often measured in a multi-channel format, e.g., multiple receivers are deployed in applications such as multi-input multi-output (MIMO) communication and radar imaging. In such cases, the overall power consumption increases with the number of radio-frequency (RF) chains, where each RF chain includes an ADC.

Among different architectures and approaches to reduce power consumption of ADCs, the following three methods have gained popularity in the recent literature:

- Time-encoding machines (TEM) [5–14].
- Unlimited/modulo sampling [17–27].
- Task-based sampling [28–35].

These approaches focus on different frameworks and aspects of ADCs to reduce power consumption. For example, the TEM architecture is an alternative to the conventional clock-based instantaneous sampling mechanism. In the TEM framework, an analog signal is discretely represented by the time instances at which the integral of the analog signal crosses a threshold. The sampling mechanism does not require a clock, as in the conventional instantaneous sampling, to control it, which makes it power efficient.

In unlimited or modulo sampling, the focus is on the dynamic range of an ADC, which plays a crucial role in determining its power consumption and a number of quantization levels. In general, the dynamic range of an ADC is higher than that of the signal, or else the sampled values which are beyond the ADC's range will be clipped. Clipping is a lossy process, and generally, high-rate high-power ADCs are used for signal reconstruction from clipped samples. To avoid clipping, the dynamic range of the ADC has to be chosen according to that of the signal. In an unlimited sampling framework, it is shown that by using a suitable analog preprocessing before sampling, high-dynamic-range signals can be sampled with lower-dynamic-range ADCs. The preprocessing operation is realized by a modulo operation where the signal is folded back to fit within the ADC's dynamic range.

Several algorithms have been suggested to reconstruct the signals from TEM and modulo measurements by using signals' priors. For example, bandlimitedness and finite rate of innovation (FRI) models are used to reconstruct signals from TEM measurements in [6] and [8], respectively. Similarly, reconstruction algorithms are proposed for modulo samples for different signal models, namely, bandlimited functions [17, 18, 20], spline spaces [36], parametric classes [37], and sparse signals [38, 39]. The previously mentioned works focus on recovering the analog signal from discrete measurements by assuming an infinite number of quantization levels. However, in many applications, the goal is to extract limited information from the digital (quantized) measurements rather than the reconstruction. For example, in a direction of arrival estimation problem, the parameters of interest are often recovered from the signal correlation, and in this case, the task is to determine the auto-correlation matrix from the measurements. In such task-limited applications, the number of measurements can be combined to reduce their dimensionality before extracting the desired information. The reduced dimensionality allows low-resolution, low-power quantizers to be used without increasing the memory requirements.

In this chapter, we discuss the abovementioned frameworks. Specifically, we focus on the theory and algorithms of these methods for different signal models and applications. Beyond theoretical underpinnings, we also discuss hardware implementations of these frameworks, which were built in our labs. For more details we refer the reader to the following weblinks:

- https://www.weizmann.ac.il/math/yonina/software-hardware/hardware.
- http://alumni.media.mit.edu/~ayush/usf.html.

1.1 Symbols and Notations

We use the following notations throughout the chapter. The set of reals, integers, and complex numbers are denoted by $\mathbb{R}$, $\mathbb{Z}$, and $\mathbb{C}$, and the set of square-integrable functions is denoted by L^2. Vectors and matrices are represented by lowercase and uppercase boldfaced letters, respectively. For a matrix $\mathbf{A}$, matrices $\mathbf{A}^T$ and $\mathbf{A}^{-1}$ denote its transpose and inverse, respectively. Trace of a matrix $\mathbf{A}$ is denoted by $\mathrm{Tr}(\mathbf{A})$. For any matrix $\mathbf{A}$, its (m, n)-th element is denoted as $(\mathbf{A})_{m,n}$. A vector $\mathrm{vec}(\mathbf{A})$ is constructed from $\mathbf{A}$ by using columnwise vectorization. The statistical expectation operator is denoted as $E[\cdot]$. For any $a \in \mathbb{R}$ and $\lambda \in \mathbb{R}^+$, the modulo operation $\mathcal{M}_\lambda(\cdot)$ is given as

$$\mathcal{M}_\lambda(a) = (a + \lambda) \bmod 2\lambda - \lambda. \tag{1}$$

Uniform samples of a signal $f(t)$ are denoted by $f(nT_s)$; The continuous-time Fourier transform of a signal $f(t)$ is denoted as $F(\omega) = \int f(t)e^{-\mathrm{j}\omega t}\mathrm{d}t$ where $\omega \in \mathbb{R}$ is in rad/sec. The discrete-time Fourier transform (DTFT) of the samples $y(nT_s)$ is given by

$$Y(e^{\mathrm{j}\omega T_s}) = \sum\nolimits_{n\in\mathbb{Z}} y(nT_s)e^{\mathrm{j}\omega T_s}.$$

1.2 Signal Models

In this chapter, we consider bandlimited and FRI signals. The set $\mathcal{B}_\Omega$ denotes bandlimited functions whose Fourier spectrum is zero outside $[-\Omega, \Omega]$. An L-th order FRI signal consisting of a stream of L pulses is given as

$$g(t) = \sum_{\ell=1}^{L} a_\ell\, h(t - \tau_\ell), \tag{2}$$

where $h(t)$ is a known pulse or a filter and the FRI parameters $\{a_\ell, \tau_\ell\}_{\ell=1}^{L}$ are a set of amplitude and time delays [1, Chapter 15][16, 40, 41]. We assume that all the quantities are real-valued. Further, we assume that $\tau_\ell \in (0, T_0]$ where the maximum time delay T_0 is known.

In the next section, we discuss time-encoding machines followed by modulo sampling in Sect. 3. In Sect. 4, we present the task-based sampling framework, and concluding remarks are discussed in Sect. 5.

2 Time-Encoding Machines

Analog signals are commonly represented by their instantaneous values measured at a set of time instants for digital processing. A continuous-time signal $f(t)$ is represented in discrete time by its samples $\{f(t_n)\}_{n\in\mathbb{Z}}$ where t_n's denote the sampling locations. Typically, the set of time instants is uniformly spaced, which results in uniform or synchronous sampling. Specifically, $t_n = nT_s$ where $T_s > 0$ is sampling interval. Uniform sampling has several advantages, such as it allows the use of standard Fourier and harmonic analysis. These analyses are useful in establishing a relationship between the samples or their spectrum with the corresponding analog signal. These relationships are used to derive bounds on the sampling rates for perfect reconstruction of the analog signals and often lead to closed-form reconstitution formulae. The Shannon-Nyquist sampling theorem for bandlimited signals is an example of a uniform sampling framework [2, 3]. Despite being a widely used approach, uniform sampling has its disadvantages. While realizing ADCs for uniform sampling, a critical concern is the requirement of a clock that controls the sampling rate. It is desirable to use a high-precision clock to reduce timing jitters. ADCs with high-precision clocks are expensive and power-consuming. In addition, clocks are prone to electromagnetic interference.

An alternative to uniform sampling is the non-uniform sampling framework [42]. Non-uniform sampling patterns can be divided into two categories: (i) non-adaptive or signal-independent, where the sampling patterns do not change for different signals within a signal class of interest, and (ii) adaptive or signal-dependent sampling, where the pattern varies from signal to signal. In the non-uniform non-adaptive sampling frameworks [43–49], the sampling locations, $\{t_n\}$, are determined in advance for a class of signals and are fixed. For example, in random sampling, the sampling locations, $\{t_n\}$, follow a certain probability distribution function that depends on the class of signals to be sampled. Few of these schemes, such as random sampling, do not require external clocks for sampling and, hence, are free of electromagnetic interference [50]. In the uniform sampling framework, knowledge of the amplitude samples $f(nT_s)$ is sufficient for recovery. However, in non-adaptive non-uniform frameworks, one must know the sampling locations t_n's together with the amplitudes $f(t_n)$ for reconstruction, which increases the amount of storage and transmission cost. Moreover, while implementing these schemes in hardware, one requires to have precise control of the sampling locations; otherwise, distortions due to timing jitter arise as in the uniform sampling framework.

On the other hand, in the signal adaptive framework, such as time-encoding sampling [5–12], the sampling locations vary with signals within a class. Unlike uniform sampling and random sampling, where the analog signal is measured at a predefined set of time instants, in time encoding, time instants are measured when the analog signal or its function crosses a predefined fixed set of amplitudes or levels. These time encodings are signal-dependent and act as a digital representation, and hence these ADCs are called time-encoding machines (TEMs). Time-encoding architectures include level-crossing methods or crossing-TEMs [9–14] and integrated and fire time-encoding machines (IF-TEMs) [5–8].

In level-crossing methods, the input signal is compared against a set of predefined functions. The time instants at which the signal crosses these functions are then recorded. A popular level-crossing sampling architecture is zero-crossing detectors where the signal is represented by its zero-crossing instants [13, 14]. Alternatively, one can use a set of constant amplitude levels for time encoding [9–12].

Another popular time-encoding framework is IF-TEMs which are inspired by the mechanism of biological neurons [5–8]. A neuron outputs a series of action potentials whose timings encode the original input in response to an input. Similarly, IF-TEM outputs signal-dependent time encodings. Compared to multi-level-crossings-based encoding, the IF-TEMs use a single threshold or level, and hence a single cooperator is required. IF-TEMs also provided better control over the sampling rate by using tunable parameters compared to a single-channel level-crossing sampler, such as zero-crossing ADC.

In the next subsection, we present theory of IF-TEM and then discuss reconstruction of bandlimited and FRI signals in the following subsections.

2.1 Theory of IF-TEM Framework

Consider a real-valued, bounded, analog signal $f(t)$. In an IF-TEM, the signal is first made positive valued by adding a bias b to it where $b > c \geq |f(t)|$. The positive signal, $b + f(t)$, is scaled by a factor $\frac{1}{\kappa}$ for some $\kappa > 0$. The scaling can be used to control the dynamic range of the signal. Then the signal $\frac{1}{\kappa}(b + f(t))$ is integrated and is compared to a threshold Δ by using a comparator (C) as illustrated in Fig. 1. When the integrated signal crosses the threshold, the time instant is recorded and the integrator is set to zero. The process is repeated to generate a monotonically increasing set of time instants $\{t_n\}_{n\in\mathbb{Z}}$, which encodes the analog signal. The input signal $f(t)$, IF-TEM parameters (b, κ, Δ), and the time encodings $\{t_n\}_{n\in\mathbb{Z}}$ are related as

$$\frac{1}{\kappa}\int_{t=t_{n-1}}^{t_n} (b + f(t))\,\mathrm{d}t = \Delta. \tag{3}$$

Since $f(t)$ is bounded, that is, $|f(t)| \leq c$, we can bound the integral in (3) and arrive at the following inequalities

$$\frac{\kappa\Delta}{(b+c)} \leq t_n - t_{n-1} \leq \frac{\kappa\Delta}{(b-c)}. \tag{4}$$

The implication is that the difference between any two consecutive firing instants is upper and lower bounded by $\frac{\kappa\Delta}{(b+c)}$ and $\frac{\kappa\Delta}{(b-c)}$, respectively. Alternatively, one can derive the maximum and minimum number of time encodings per second or *firing rates* (FR) as

$$\mathrm{FR}_{\max} = \frac{(b+c)}{\kappa\Delta}, \quad \text{and} \quad \mathrm{FR}_{\min} = \frac{(b-c)}{\kappa\Delta}, \tag{5}$$

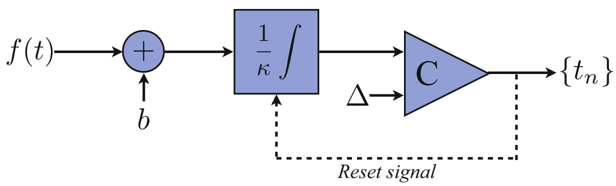

Fig. 1 A schematic of IF-TEM: A signal $f(t)$ is represented by time encodings $\{t_n\}$

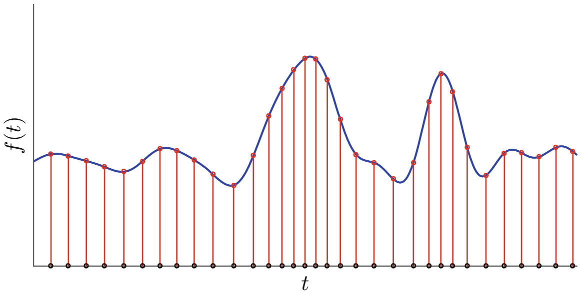

Fig. 2 Time encodings of a bandlimited signal $f(t)$: Time encodings are dense in regions of large amplitude variations compared to low-variation regions

respectively. The firing rate is equivalent to the sampling rate in a uniform sampling framework or sampling density in a non-uniform sampling case. But unlike in uniform sampling or random sampling, the firing rate is not fixed and is signal dependent.

In Fig. 2, we illustrate sampling instants of a bandlimited function $f(t)$ (in blue), which are measured via an IF-TEM. In particular a set of time encodings $\{t_n\}$ are generated by using an IF-TEM for $f(t)$ and measurements $\{t_n, f(t_n)\}$ are plotted together with $f(t)$. We observe that the signal is densely sampled when the amplitude varies sharply compared to the slowly varying regions. This illustrates the signal-dependent nature of IF-TEM measurements. Depending upon the signal reconstruction approach, the variation of the firing rate between its minimum and maximum values may be an undesirable feature of IF-TEM. For example, as discussed in the subsequent sections, there exists an algorithm to reconstruct bandlimited signals from their time encodings, provided that the minimum firing rate is below the Nyquist rate. By choosing the IF-TEM parameters (b, κ, Δ), one can adjust the minimum firings to satisfy such conditions. Hence, by following (4), the time encodings might have a much higher density compared to the Nyquist rate, which amounts to a larger number of measurements compared to uniform sampling. A similar oversampling is also noted while reconstructing any non-uniform samples by using iterative reconstruction algorithms (cf. [51, Th. 8.13]).

An important question is whether $f(t)$ can be reconstructed from its time encodings $\{t_n\}_{n\in\mathbb{Z}}$ by adjusting the IF-TEM parameters. It was shown that perfect reconstruction is possible for bandlimited and FRI signals as long as $\mathrm{FR}_{\min}$ is above the Nyquist rate or rate of innovation [6, 8, 52, 53]. Before that, we first discuss a general philosophy for reconstruction.

Following average values of the signal $f(t)$ can be measured by rearranging (3):

$$y_n = \int_{t=t_{n-1}}^{t_n} f(t)\,\mathrm{d}t = \kappa\Delta - b(t_n - t_{n-1}). \tag{6}$$

The set of average values, $\{y_n\}_{n\in\mathbb{Z}}$, are an alternative discrete representation of $f(t)$. If $f(t)$ is differentiable, then by using the mean value theorem, we have from (6)

$$\frac{y_n}{t_n - t_{n-1}} = \frac{1}{t_n - t_{n-1}} \int_{t=t_{n-1}}^{t_n} f(t)\,\mathrm{d}t = f(t'_n), \tag{7}$$

where $t'_n \in [t_{n-1}, t_n]$. This implies that for smooth signals, non-uniform, instantaneous samples can be measured from the time encodings and IF-TEM parameters.

Given $\{t'_n, f(t'_n)\}_{n\in\mathbb{Z}}$, one can directly apply existing algorithms for signal reconstruction from non-uniform samples provided that the sampling locations satisfy the desired density criteria [51, Ch. 8]. Alternatively, one can use signal's average values $\{y_n\}$ to reconstruct the smooth signals (see Ch. 8 in [51] for details). Reconstruction from the average values is the basic approach algorithms use to reconstruct different classes of signals from their time encoding. We shall discuss these algorithms for bandlimited and FRI signals in the next two subsections.

2.2 Reconstruction Algorithm for Bandlimited Signals

In this subsection, we consider finite-energy, bandlimited signals and discuss their reconstruction from time encodings. Specifically, the signals considered are in $\mathcal{B}_\Omega \cap L^2(\mathbb{R})$ (Paley–Wiener class). For bandlimited signals, a perfect reconstruction algorithm was proposed by Lazar and Tóth [6]. The algorithm is iterative, and in each successive iteration, it approximates a bandlimited function by using the average measurements from the previous iteration. An operator that projects the average values to $\mathcal{B}_\Omega \cap L^2(\mathbb{R})$ is defined as

$$\mathrm{B}_\Omega f(t) = \sum\nolimits_{n\in\mathbb{Z}} y_n\, h(t-\tau_n), \tag{8}$$
$$f(t) = \sum\nolimits_{n\in\mathbb{Z}} y_n\, h(t-\tau_n), \qquad f \in \mathrm{B}_\Omega$$

where $\tau_n = \frac{t_{n-1}+t_n}{2}$ and $h(t) = \frac{\sin(\Omega t)}{\pi t}$ is the lowpass filter corresponding to the bandlimited space $\mathcal{B}_\Omega$. The operator outputs a bandlimited signal by summing shifted sinc functions similar to the standard Shannon-Nyquist reconstruction framework for uniform samples. However, the shifts are not uniform and are placed midway between two consecutive firing instants. High-density firing rates occur when $f(t)$ varies rapidly. This, in turn, results in large values of average values y_ns (cf. (6)) and high-density shift values $\{\tau_n\}$. From (8), we observe that the operators are densely placed with larger weights in such high-density regions. Similarly, when $f(t)$ is slowly varying, delayed copies of $h(t)$s are placed far from each other with small weights. In this way, the operator produces a good approximation of $f(t)$ from the time encodings.

Starting from the approximation $f_0(t) = \mathrm{B}_\Omega f(t)$, an iterative algorithm is proposed where the approximation at the k-th iteration is

$$f_k(t) = f_{k-1}(t) + \mathrm{B}_\Omega\left(f(t) - f_{k-1}(t)\right). \tag{9}$$

Then, by using the principle of induction, we have that [54]

$$f_k(t) = \sum_{l=0}^{k} (\mathcal{I} - \mathrm{B}_\Omega)^l \, \mathrm{B}_\Omega f(t), \tag{10}$$

where $\mathcal{I}$ is an identity operator. If $\|\mathcal{I} - \mathrm{B}_\Omega\|_{L^2} < 1$ then the operator B_Ω is invertible. By using the Neumann series representation, the inverse is expanded as

$$\mathrm{B}_\Omega^{-1} = \sum_{l=0}^{\infty} (\mathcal{I} - \mathrm{B}_\Omega)^l. \tag{11}$$

Hence, if $\|\mathcal{I} - \mathrm{B}_\Omega\|_{L^2} < 1$, we have the following convergence

$$\lim_{k\to\infty} f_k(t) = \sum_{l=0}^{\infty} (\mathcal{I} - \mathrm{B}_\Omega)^l \, \mathrm{B}_\Omega f(t) = \mathrm{B}_\Omega^{-1} \mathrm{B}_\Omega f(t) = f(t). \tag{12}$$

The IF-TEM parameters can be chosen to ensure that the norm is bounded. In particular, it can be shown that

$$\|\mathcal{I} - \mathrm{B}_\Omega\|_{L^2} \leq \frac{\kappa \Delta}{(b-c)} \frac{\Omega}{\pi}. \tag{13}$$

If the parameters are chosen such that

$$\frac{\Omega}{\pi} < \frac{(b-c)}{\kappa \Delta}, \tag{14}$$

then the norm condition is satisfied and the algorithm converges. The quantity $\frac{\Omega}{\pi}$ is the Nyquist rate (in Hz) for the signals in $\mathcal{B}_\Omega$. Hence the inequality (14) signifies that the minimum firing rate of the IF-TEM (cf. (5)) should be strictly greater than the Nyquist rate.

It can be shown that

$$\|f(t) - f_k(t)\|_{L^2} \leq \left(\frac{\kappa \Delta}{(b-c)} \frac{\Omega}{\pi} \right)^{(k+1)} \|f(t)\|_{L^2}. \tag{15}$$

This inequality allows the determination of the number of iterations required to achieve desired reconstruction accuracy. The recovery approach is summarized in the following theorem.

Theorem 1 (Bandlimited Signal Recovery Using IF-TEM [6]) *Consider a bandlimited signal* $f(t) \in \mathcal{B}_\Omega \cap L^2(\mathbb{R})$ *with* $|f(t)| < c$*. Let* $\{t_n\}$ *denote a set of time encodings for* $f(t)$ *which are measured from an IF-TEM with parameters* (b, κ, Δ) *(see Fig. 1). Let* $f_k(t)$ *be given as in* (10)*. Then*

$$\lim_{k\to\infty} f_k(t) = f(t), \tag{16}$$

provided that

$$\frac{\Omega}{\pi} < \frac{(b-c)}{\kappa\Delta}. \tag{17}$$

The recovery methods from IF-TEM observations require that the input has a restricted amplitude $|f(t)| \leq c$. Recently, it was shown that the input amplitude could be extended beyond this range without changing the IF-TEM parameters by applying a modulo nonlinearity [24, 27].

Multi-channel extension of IF-TEM sampling for bandlimited signals is considered in [55–57]. It is shown that each channel can operate at a much lower rate than the single-channel framework as in the conventional multichannel sampling scheme. Lowrate IF-TEMs in each channel reduce the power requirements. An extension to signals in shift-invariant spaces is presented in [58]. Next, we discuss IF-TEM sampling for FRI signals.

2.3 Reconstruction of FRI Signals

FRI signals, as in (2), use a sampling kernel prior to ADC, which facilitates sub-Nyquist sampling [1]. Specifically, the filter acts as an anti-aliasing filter during the sampling process and aids in reconstruction (see [59–61, Chapter 15]). Hence before discussing sampling of FRI signals by IF-TEM, we first discuss sub-Nyquist aspects of FRI signals.

Sub-Nyquist Sampling of FRI Signals

The FRI parameters are typically estimated from frequency domain samples [1, 16, 62]. Consider the FRI signal model in (2). Let $G(k\omega_0)$ and $H(k\omega_0)$ be uniform samples of the Fourier transforms of the FRI signal $g(t)$ and pulse $h(t)$, respectively. Here, ω_0 is the sampling interval in the Fourier domain and $k \in \mathcal{K} \subset \mathbb{Z}$ is the sample index set. Then by assuming that $H(k\omega_0) \neq 0$ it can be shown that

$$S(k\omega_0) = \frac{G(k\omega_0)}{H(k\omega_0)} = \sum_{\ell=1}^{L} a_\ell\, e^{-\mathrm{j}k\omega_0\tau_\ell}, \quad k \in \mathcal{K}. \tag{18}$$

These measurements in the form of a sum of exponentials and high-resolution spectral estimation (HRSE) methods can be applied to determine $\{a_\ell, \tau_\ell\}_{\ell=1}^{L}$ from them [63, Ch. 4] [64–67]. The estimation is unique provided that $\omega_0 = \frac{2\pi}{T_0}$ and $\mathcal{K}$ is a set of consecutive integers with $|\mathcal{K}| \geq 2L$. Further, by assuming that the time delays are on a grid, compressive sensing (CS) approaches can also be applied to determine the FRI parameters [68]. Unlike HRSE approaches, in the CS-based reconstruction, $\mathcal{K}$ need not be a set of consecutive integers and the condition $|\mathcal{K}| \geq 2L$ is sufficient.

Since $H(k\omega_0)$ can be computed in advance from the known pulse $h(t)$, one has to determine $\{G(k\omega_0)\}_{k\in\mathcal{K}}$ for constructing the measurements as in (18) and subsequent estimation of FRI parameters. These Fourier samples can be determined by time samples by using a sum-of-sincs (SoS) filter prior to sampling [16, 62]. To keep the response of the filters to be real-valued, we choose the set $\mathcal{K}$ as $\{-K, \cdots, K\}$ where $K \geq L$. The response of the SoS filter to the FRI signal in (2) is given as

$$f(t) = \sum_{k=-K}^{K} G(k\omega_0)\, e^{\mathrm{j}k\omega_0 t}. \tag{19}$$

Then from uniform samples of $f(t)$, the Fourier samples $G(k\omega_0)$ can be determined provided that there are at least $2K+1$ samples and the sampling interval is less than or equal to $\frac{T_0}{2K+1}$.

Note that $f(t)$ is a periodic bandlimited signal or a trigonometric polynomial (TP) of order K. For $K \geq L$, all the information of the FRI signal $g(t)$ resides in $f(t)$ in terms of the Fourier samples. Hence, any sampling framework that ensures perfect recovery of $f(t)$ from its measurements is also applicable for the reconstruction of FRI signals. Next, we discuss the IF-TEM sampling framework for FRI signals.

IF-TEM Sampling

As in the bandlimited case, FRI signals can be reconstructed from time encodings [8, 52, 53, 69, 70]. Different sampling kernels can be used prior to IF-TEM sampling, such as polynomial generating kernels [69], hyperbolic functions [70], and the SoS kernel [8, 53]. In the following, we discuss sampling using an SoS kernel and so that the input to the IF-TEM is given as in (19). The main results of this section are summarized in the following theorem [8, 52].

Theorem 2 *Consider a L-th order FRI signal $g(t)$ as in (2) its filtered response $f(t)$ as in (19). Consider the sampling mechanism shown in Fig. 1 where TEM parameters $\{b, \kappa, \delta\}$ are real and positive with $b > c = \|f(t)\|_\infty$ and*

$$\frac{b-c}{\kappa\delta} \geq \frac{2K+2}{T_0}. \tag{20}$$

Then, the parameters $\{a_\ell, \tau_\ell\}_{\ell=1}^{L}$ can be perfectly recovered from the TEM outputs if $K \geq L$.

We discuss a brief outline of the proof (see [8] for a detailed proof). Since $f(t)$ is a K-th order TP, the results discussed in this section are also applicable to the problem of sampling and reconstruction of trigonometric polynomials by using IF-TEM.

To generate the time encodings, bias $b > c = \|f(t)\|_\infty$ is added to $f(t)$; then the sum is scaled by $\frac{1}{\kappa}$, integrated, and compared against threshold Δ as discussed earlier. Since $f(t)$ is periodic with time period T_0, we focus on the time encodings in an interval of length T_0. Let there be N time encodings $\{t_n\}_{n=1}^N$ within an interval of length T_0. Substituting (19) in (6), we have

$$y_n = \sum_{\substack{k=-K \\ k\neq 0}}^{K} G(k\omega_0) \frac{e^{\mathrm{j}k\omega_0 t_n} - e^{\mathrm{j}k\omega_0 t_{n-1}}}{\mathrm{j}k\omega_0} + G(0)\,(t_n - t_{n-1}), \tag{21}$$

for $n = 2, \cdots, N$. We can rewrite the measurements in matrix form as

$$\mathbf{A}\mathbf{g} = \mathbf{y}, \tag{22}$$

where

$$\mathbf{A} = \begin{pmatrix} e^{-\mathrm{j}K\omega_0 t_2} - e^{-\mathrm{j}K\omega_0 t_1} & \cdots & t_2 - t_1 & \cdots & e^{\mathrm{j}K\omega_0 t_2} - e^{\mathrm{j}K\omega_0 t_1} \\ e^{-\mathrm{j}K\omega_0 t_3} - e^{-\mathrm{j}K\omega_0 t_2} & \cdots & t_3 - t_2 & \cdots & e^{\mathrm{j}K\omega_0 t_3} - e^{\mathrm{j}K\omega_0 t_2} \\ \vdots & \ddots & \vdots & \ddots & \vdots \\ e^{-\mathrm{j}K\omega_0 t_N} - e^{-\mathrm{j}K\omega_0 t_{N-1}} & \cdots & t_N - t_{N-1} & \cdots & e^{\mathrm{j}K\omega_0 t_N} - e^{\mathrm{j}K\omega_0 t_{N-1}} \end{pmatrix}, \tag{23}$$

$\mathbf{g} = [G(-K\omega_0), \cdots, G(0), \cdots, G(K\omega_0)]^{\mathrm{T}}$, and $\mathbf{y} = [y_2, \cdots, y_N]^{\mathrm{T}}$. In [8], it is shown that the matrix $\mathbf{A}$ is left invertible if $N \geq 2K + 2$, and hence the Fourier samples $\mathbf{g}$ can be computed from the time encodings as $\mathbf{A}^\dagger \mathbf{y}$. Then the FRI parameters can be determined from the Fourier using HRSE methods. The condition $N \geq 2K + 2$ implies that there should be at least $2K + 2$ firings within an interval of length T_0. This can be ensured by choosing the IF-TEM parameters such that the minimum firing rate is greater than $\frac{2K+2}{T_0}$, that is,

$$\frac{b - c}{\kappa\Delta} \geq \frac{2K + 2}{T_0}, \tag{24}$$

where $K \geq L$. Simulation results for reconstruction of an FRI signal consisting of three third-order b-splines are shown in Fig. 3. Perfect reconstruction is achieved from the IF-TEM measurements.

Since the estimation of the Fourier coefficients requires the inversion of the matrix $\mathbf{A}$, it is desirable to have a stable inverse, especially when the time encodings are perturbed. In [8], it was shown that if the trigonometric polynomial $f(t)$ in (19) does not include the term corresponding to $k = 0$, then the resulting matrix is more stable than $\mathbf{A}$. This can be achieved by designing an SoS filter that excludes the zeroth frequency. The resulting matrix will have a Vandermonde structure, and it is

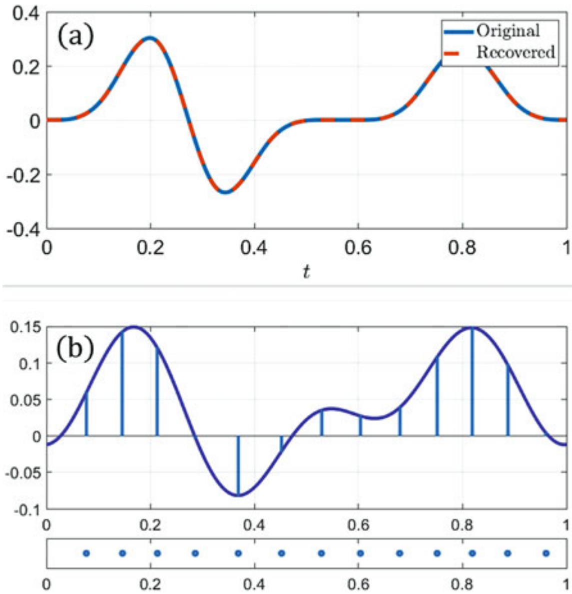

Fig. 3 Sampling and reconstruction of a stream of pulses using IF-TEM by applying the SoS kernel. (**a**): the input signal and its reconstruction for $L = 3$. (**b**): the filtered signal $f(t)$ and the time instants t_n for $L = 3$ [8]

left invertible if $N \geq 2K + 1$. With the exclusion of the zeroth frequency, $K \geq 2L$ to estimate a set of $2L$ consecutive Fourier samples. This, in turn, increases the firing rate as it is proportional to K (cf. (24)). However, in the presence of noise or perturbations in the time encodings, both with and without zero approaches require a larger number of measurements to achieve a desirable accuracy. In this case, it is shown that the without-zero approach results in a lower error in the estimation of time delays compared to the with-zero approach for the same number of measurements [8]. An alternative is to assume that the time delays are on a grid and use CS methods for reconstruction. For both off-grid and on-grid time delays, the without-zero approach results in a lower reconstruction error than the with-zero approach for the same number of samples.

2.4 TEM Hardware

A hardware prototype of an IF-TEM-based sub-Nyquist sampler for FRI signals was developed in the SAMPL lab https://www.weizmann.ac.il/math/yonina/software-hardware/hardware and demonstrated in [71]. A prototype of the hardware board is shown in Fig. 4. The board acts as an ADC, which is based on the IF-TEM principle and has a bias and threshold. The scaling factor, κ, is set as unity. In this demonstration, FRI signals of bandwidth 20 MHz (the Nyquist rate $\geq$40 MHz) are generated, and a lowpass filter with a cutoff frequency of 0.5 MHz is used as a sampling kernel. The filtered signal is then discretized by using the IF-TEM module

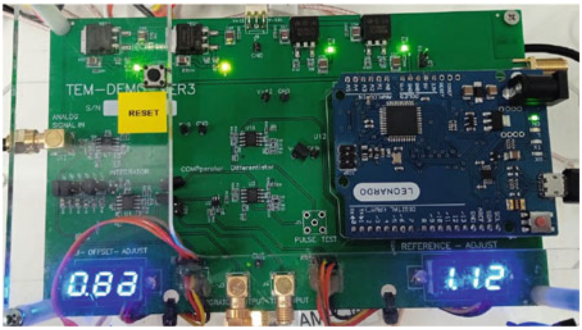

Fig. 4 A hardware prototype board of IF-TEM sampler developed in SAMPL Lab [71]. For further details, refer to the webpage: https://www.weizmann.ac.il/math/yonina/software-hardware/hardware

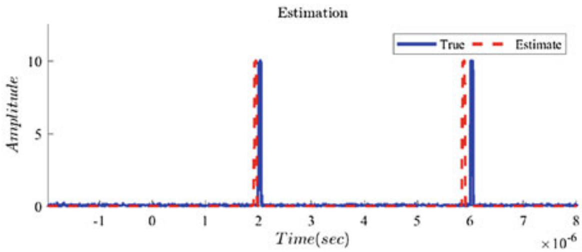

Fig. 5 Reconstruction of FRI pulses by using the hardware board shown in Fig. 4

shown in Fig. 4 by selecting appropriate values of bias and threshold. In the demo setup, the maximum firing rate is 1.6 MHz. From the measured time encodings, the FRI parameters are estimated by using the algorithm derived in [8]. The true FRI pulses and the reconstructed ones are shown in Fig. 5. We observe that FRI signals were reconstructed from IF-TEM encodings with a firing rate that is 12.5 times less than the Nyquist rate. Hence, sub-Nyquist sampling is possible with an IF-TEM. Another relevant point is that the hardware does not use any clock, unlike conventional ADCs, which makes it power efficient and immune to any electromagnetic interference.

3 Modulo Sampling

We now turn to discuss modulo sampling with the aim of sampling signals with low-dynamic range ADCs without losing any information due to saturation. Saturation occurs when the analog signal exceeds the dynamic range of the ADC, and it results in clipped measurements. Clipped measurements via ADC saturation pose severe challenges in a variety of applications such as *high-dynamic-range* (HDR) photography [72], autonomous navigation [73], radar imaging [74], seismic imaging [75], communication systems [76], ultrasound imaging [77], music signal processing [78], and more. A simple solution to avoid clipping is to increase the dynamic range of the ADC. However, high-dynamic-range ADCs require high power to operate. Moreover, they require a large number of quantization levels to accurately represent the samples which in turn increases the memory requirements.

Due to the widespread nature of the clipping problem, several papers have studied this problem in different contexts [77–86]. These approaches are based on *hardware-only* or *algorithms-only* solutions. In particular, hardware-based solutions tackle the dynamic range problem at the electronic level, and they do not leverage the potential benefits of algorithms [79–81]. This amounts to sophisticated hardware architectures, such as automatic gain control, that require application-specific tailoring. On the other hand, algorithm-based de-clipping is based on signal interpolation, inpainting, or optimization [77, 78, 82–86] where the goal is to recover lost samples under certain assumptions, typically related to the smoothness of the underlying signal. A drawback of the algorithm-based de-clipping is that theoretical guarantees are largely unexplored. For instance, the question of overcoming clipping by oversampling has no clear answer.

To overcome the dynamic range bottleneck, the unlimited sampling or modulo sampling framework was recently introduced in [17–27]. In this framework, a modulo operation is applied prior to sampling to restrict the signal's dynamic range by folding it. This operation is realized in the hardware. The folded or modulo signal is then sampled by using an ADC such as a conventional instantaneous sampler [17–23] or a TEM [24, 27]. Since the modulo operation is nonlinear, the modulo samples are distorted versions of the true (unfolded) samples. However, the distortion is structured, and this fact, together with the signal model, is used for recovering unfolded samples from the folded ones. Recovery algorithms vary based on how they exploit the distortion and signal model. In the following, we discuss the modulo sampling framework in the context of bandlimited and FRI signals. We discuss theoretical aspects, recovery algorithms, and hardware prototypes.

3.1 Theory of Modulo Sampling

Consider a real-valued, analog signal $f(t)$. The objective is to sample the signal by using an ADC which has a dynamic range $[-\lambda, \lambda]$ for some known $\lambda > 0$. By considering a conventional uniform-sampling ADC framework, the samples of the ADC are given by $\text{sgn}(f(nT_s)) \max(\lambda, |f(nT_s)|)$ where $\text{sgn}(f(nT_s))$ denotes the sign of the measurement. In this case, when the samples are beyond the dynamic range of the ADC, they are clipped, and the output is $\lambda\, \text{sgn}(f(nT_s))$.

To avoid clipping, a modulo operation is used prior to sampling, as shown in Fig. 6. The output of the modulo operator $f_\lambda(t) = \mathcal{M}_\lambda(f(t))$ is sampled to obtain the measurements $f_\lambda(nT_s)$. The modulo operator, together with the sampler, is termed modulo-ADC. Unlike the conventional ADC, modulo-ADC accommodates signals which are beyond its dynamic range and information is not lost due to clipping. A comparison of the two sampling frameworks is shown in Fig. 7. Depending on the signal class, a sampling kernel can be used prior to the modulo operation. For example, for the reconstruction of signals in shift-invariant spaces,

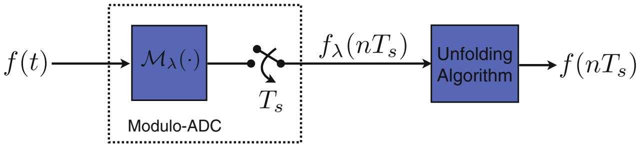

Fig. 6 Modulo sampling framework: Signal $f(t)$ is folded by modulo operation before sampling to avoid clipping. The folded signal is sampled, and an unfolding algorithm is applied to determine the actual samples from folded ones for further processing

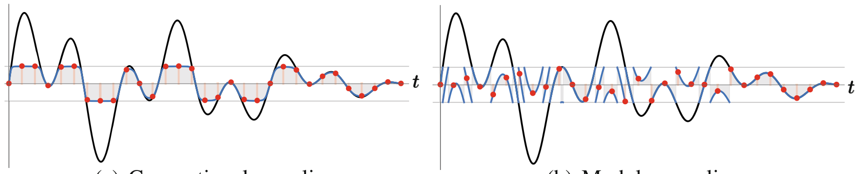

Fig. 7 Demonstration of conventional sampling with clipping and modulo sampling: (**a**) Conventional sampling: Original signal (in black) is clipped (in blue) when it crosses the dynamic range of the ADC. The clipped samples are shown in red. (**b**) The original signal (in black) is folded back (in blue) to avoid clipping, and samples of the folded signal (in red) are measured

prefiltering is applied [36] before the modulo operation. During reconstruction, unfolded samples $f(nT_s)$ are determined by the folded samples $f_\lambda(nT_s)$ by applying an unfolding algorithm. These algorithms may differ from each other in terms of their working principle, but most of them use the fact that the modulo signal $f_\lambda(t)$ can be decomposed as

$$f_\lambda(t) = f(t) + z(t), \tag{25}$$

where the *residual signal* $z(t)$ is a piecewise constant signal whose values are integer multiple of 2λ. The transition times between pieces of $z(t)$ indicate locations at which $f(t)$ is folded. Mathematically, $z(t)$ can be written as

$$z(t) = \sum_{q=1}^{Q} d_q\, u(t - \tau_q), \tag{26}$$

where $d_q \in 2\lambda\mathbb{Z}$ and $u(t)$ is step function. Folding instances are denoted by τ_q. The number of foldings, Q, could be either finite or countably infinite depending on the signal $f(t)$. Hence, $z(t)$ is structured and depends on $f(t)$. This decomposition, or specific structure of $z(t)$, is used together with signal priors for reconstruction.

In the following section, we discuss modulo sampling for bandlimited signals and then present results for periodic bandlimited signals.

3.2 Modulo Sampling for Bandlimited Signals

We consider the problem of reconstructing a bandlimited signal $f(t) \in \mathcal{B}_\Omega \cap L^2(\mathbb{R})$ from its modulo samples. To this end, first, the samples $f(nT_s)$ are recovered from $f_\lambda(nT_s)$ by using an *unfolding* algorithm and then $f(t)$ is recovered by using Shannon-Nyquist interpolation. For perfect reconstruction of $f(t)$ from $f(nT_s)$, it is required to sample at or above the Nyquist rate. The question is whether sampling at or above is also sufficient to unfold. Or, what should be the sampling rate (independent of any algorithm) to uniquely identify $f(t)$ from modulo samples $f_\lambda(nT_s)$? The answer to the question is given in the following theorem [21, 87].

Theorem 3 (Identifiability of Bandlimited Signals from Modulo Samples) *Any $f(t) \in \mathcal{B}_\Omega \cap L^2(\mathbb{R})$ is uniquely determined by its uniform-modulo samples measured at a rate greater than the Nyquist rate.*

For unfolding, Itoh suggested an algorithm for smooth signals in the context of phase unwrapping [88]. It was shown that if the first-order differences of the unfolded samples are bounded by λ, then unfolding can be achieved up to a constant which is multiple of 2λ [88]. However, it was unclear how to choose the sampling rate while applying the algorithm for bandlimited signals. In [17, 18], the authors proposed a higher-order version of Itoh's approach and showed that bandlimited samples could be unfolded provided that a minimum sampling density condition is satisfied. The algorithm requires a high amount of oversampling (almost 17 times higher than the Nyquist rate), but the sampling rate is independent of the dynamic range of the ADC. A λ-dependent but sampling-efficient and robust unfolding technique is proposed in [22]. Next, we present a few details of these two approaches.

Higher-Order-Difference (HoD)-Based Algorithm

From the decomposition in (25), the modulo samples can be written as

$$f_\lambda(nT_s) = f(nT_s) + z(nT_s). \tag{27}$$

Let Δ^N be the N-th order difference operator. Then by applying Δ^N followed by $\mathcal{M}_\lambda$ to $f_\lambda(nT_s)$ in (27), we have the following set of equalities:

$$\begin{aligned}\mathcal{M}_\lambda(\Delta^N f_\lambda(nT_s)) &= \mathcal{M}_\lambda(\Delta^N f(nT_s) + z(nT_s)), \\ &= \mathcal{M}_\lambda(\mathcal{M}_\lambda(\Delta^N f(nT_s)) + z(nT_s)),\end{aligned} \tag{28}$$

where we used the additive property of the modulo operator and the fact that $\mathcal{M}_\lambda(z(nT_s)) = 0$ while going from the first to the second equality. If we choose the sampling rate such that

$$|\Delta^N f(nT_s)| \leq \lambda, \tag{29}$$

then from (28) we have that

$$\mathcal{M}_\lambda(\Delta^N f_\lambda(nT_s)) = \Delta^N f(nT_s). \tag{30}$$

The relationship suggests that higher-order differences of the true samples can be computed from modulo samples. One can think of applying a N-th order anti-difference or cumulative-sum operator S^N to $\Delta^N f(nT_s)$ to determine $f(nT_s)$. But $\mathrm{S}^N \Delta^N f(nT_s) \neq f(nT_s)$ as polynomials are in the null space of S^N. To circumvent this issue, S^N is applied to $\Delta^N z(nT_s)$ which is computed from modulo samples as

$$\begin{aligned}\Delta^N z(nT_s) &= \Delta^N f_\lambda(nT_s) - \Delta^N f(nT_s),\\ &= \Delta^N f_\lambda(nT_s) - \mathcal{M}_\lambda(\Delta^N f_\lambda(nT_s)),\end{aligned} \tag{31}$$

where (28) and (30) are used to derive the above relationship. In this case too, $z(nT_s)$ are determined up to a polynomial ambiguity from $\mathrm{S}^N \Delta^N z(nT_s)$. The ambiguity can be removed up to a constant multiple of 2λ by using the fact that $z(nT_s)$ is an integer multiple of 2λ. Then $f(nT_s)$ is computed using (27).

The unfolding discussed is possible only if (29) holds. The following theorem states conditions such that the inequality (29) is satisfied [17, 18].

Theorem 4 *Consider a bounded bandlimited signal $f(t) \in \mathcal{B}_\Omega \cap L^2(\mathbb{R})$ such that $\beta_f \geq \|f(t)\|_\infty$ and $\beta_f \in 2\lambda\mathbb{Z}$. Then for any integer N and sampling interval T_s chosen such that*

$$N^\star \geq \left\lceil \frac{\log \lambda - \log \beta_f}{\log (T_s \Omega e)} \right\rceil, \tag{32}$$

and

$$T_s \leq \frac{1}{2\Omega e}, \tag{33}$$

ensures $\|\Delta^N f(nT_s)\| \leq \lambda$.

From (33), we see that the sampling rate is independent of λ. Nevertheless, compared to the Nyquist rate $\frac{\Omega}{\pi}$, the HoD-based unfolding algorithm works for oversampling factor (OF) of $2\pi e$ or 17 times above the Nyquist rate. In addition, the method is often not stable in the presence of noise due to HoD.

To address these issues, in [22], an iterative algorithm is suggested which is stable in the presence of noise and operates at lower sampling rates, as discussed next. The algorithm recovers the residual signal by using information beyond the signal's bandwidth, and hence it is termed the beyond-bandwidth residual-recovery (B^2R^2) algorithm.

B^2R^2 Algorithm

The algorithm relies on the following two properties of finite energy BL signals [22].

- Time-domain separation [21]: By using the Riemann-Lebesgue Lemma, it can be shown for any $\lambda > 0$ there exists an integer N_λ such that $|f(nT_s)| < \lambda$, for all $|n| > N_\lambda$. Hence, for $|n| > N_\lambda$, we have $f_\lambda(nT_s) = f(nT_s)$ and $z(nT_s) = 0$. Thus the modulo samples are equal to the true samples over a set of indices.
- Fourier-domain separation: Let the signal be sampled above the Nyquist rate with the sampling rate $\Omega_s > \frac{\Omega}{\pi}$. Then by applying DTFT to $f_\lambda(nT_s)$, we have that

$$F_\lambda(e^{\mathrm{j}\omega T_s}) = Z(e^{\mathrm{j}\omega T_s}), \quad \text{for} \quad \Omega < |\omega| < \Omega_s/2. \tag{34}$$

  Here we used bandlimitedness of $f(t)$ which implies that $F(e^{\mathrm{j}\omega T_s}) = 0$, for $\Omega < |\omega| < \Omega_s/2$. The relationship (34) implies that the DTFT of the true samples and that of the residual can be differentiated by oversampling.

Combining the separation properties in the two domains, the following relationship is derived:

$$F_\lambda(e^{\mathrm{j}\omega T_s}) = \sum_{n=-N_\lambda}^{N_\lambda} z(nT_s)e^{-\mathrm{j}nT_s\omega}, \quad \text{for} \quad \Omega < |\omega| < \Omega_s/2. \tag{35}$$

From (35), $z(nT_s)$can be determined by sampling $F_\lambda(e^{\mathrm{j}\omega T_s})$ at $2N_\lambda + 1$ points over the interval $\rho = (-\Omega_s/2, -\Omega) \cup (\Omega, \Omega_s/2)$ and inverting the resulting set of linear equations. Then the true samples may be recovered by using (25). However, in practice, the inversion may not be stable in the presence of noise. To overcome this issue, an iterative algorithm is proposed as a solution to the following optimization problem [22]:

$$\min_{\mathbf{z}} \quad \mathrm{C}(\mathbf{z}) = \frac{1}{2}\|\mathcal{F}_\rho(\mathbf{f}_\lambda - \mathbf{z})\|^2 \quad \text{s.t.} \quad \mathbf{z} \in \mathcal{S}_{N_\lambda}, \tag{36}$$

where $\mathcal{F}_\rho(\mathbf{f}_\lambda - \mathbf{z}) = \sum_{n\in\mathbb{Z}}(f_\lambda(nT_s) - z(nT_s))\, e^{-\mathrm{j}\omega nT_s}$, $\omega \in \rho$, and $\mathcal{S}_{N_\lambda}$ denotes sequences that have support over $\{-N_\lambda, \cdots, N_\lambda\}$. In this formulation, vectors $\mathbf{f}_\lambda$ and $\mathbf{z}$ denote vector forms of $f_\lambda(nT_s)$ and $z(nT_s)$, respectively. The optimization problem can be solved by projected gradient descent (PGD) method where starting from an initial point $\mathbf{z}^0 \in \mathcal{S}_{N_\lambda}$, the steps at the k-th iteration are

$$\begin{aligned} \mathbf{y}^k &= \mathbf{z}^{k-1} - \gamma_k \nabla \mathrm{C}(\mathbf{z}^{k-1}), \\ \mathbf{z}^k &= P_{\mathcal{S}_{N_\lambda}}(\mathbf{y}^k). \end{aligned} \tag{37}$$

In these steps, $\gamma_k > 0$ is a suitable step-size, $\nabla\mathrm{C}(\mathbf{z}) = \mathcal{F}_\rho^*\mathcal{F}_\rho(\mathbf{z} - \mathbf{f}_\lambda)$ is the gradient of $\mathrm{C}(\mathbf{z})$, and $P_{\mathcal{S}_{N_\lambda}}(\mathbf{y})$ is the orthogonal projection onto $\mathcal{S}_{N_\lambda}$. The function $\mathrm{C}(\mathbf{z})$ is convex as it is a quadratic norm over a convex set $\mathcal{S}_{N_\lambda}$. Hence, the PGD algorithm converges to the global minimum. The estimation accuracy can be improved further by rounding the solution of the optimization problem to the nearest integer multiple of 2λ as $\mathbf{z} \in 2\lambda\mathbb{Z}^{2N_\lambda+1}$.

In addition to HoD and B^2R^2 algorithms, Romanov and Ordentlich proposed a Chebyshev-polynomial-based recovery algorithm. The algorithm uses the time-domain separation property and shows that the samples $\{f(nT_s)\}_{n=-N_\lambda}^{N_\lambda}$ can be recovered from the samples $f(nT_s), n < N_\lambda$ by linear prediction. Note that for $n < N\lambda$, the samples are within the dynamic range of the ADC and hence $f_\lambda(nT_s) = f(nT_s)$. The prediction filter is designed by using the Chebyshev polynomial.

In the HoD approach, a high OF is required to ensure that the higher-order difference of the samples of the BL signal is bounded by 2λ. In contrast, both B^2R^2 and Chebyshev approaches are independent of higher-order differences and require lower oversampling. For example, in Fig. 8 we compare HoD, the Chebyshev, and B^2R^2 algorithms in terms of mean-squared error (MSE) in reconstruction for different values of OF. For signal-to-noise ratio (SNR) of 15 dB, the Chebyshev and B^2R^2 algorithms result in lower reconstruction error (in terms of MSE) as compared to the HoD method for different values of OF as observed in Fig. 8. Next, comparing B^2R^2 and Chebyshev approaches (see Fig. 9), we observe that the B^2R^2 approach has lower MSE for a given OF, λ, and noise level (see [22] for more details).

3.3 Modulo Sampling for FRI Signals

Compared to the bandlimited signal model, there are a limited number of results for FRI signal reconstruction from modulo samples. Of course, one can extend the bandlimited signal results by considering a lowpass sampling kernel for FRI

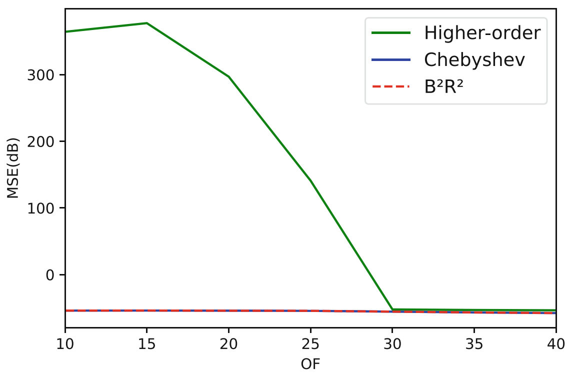

Fig. 8 Comparison of algorithms in terms of MSE in recovering a bandlimited signal from modulo samples with $\lambda = 0.025$, and SNR = 25 dB. The higher-order difference approach has an error of -60 dB for OF ≥ 30, whereas the remaining methods are able to achieve -60 dB error for OF = 10 (see [22] for more details)

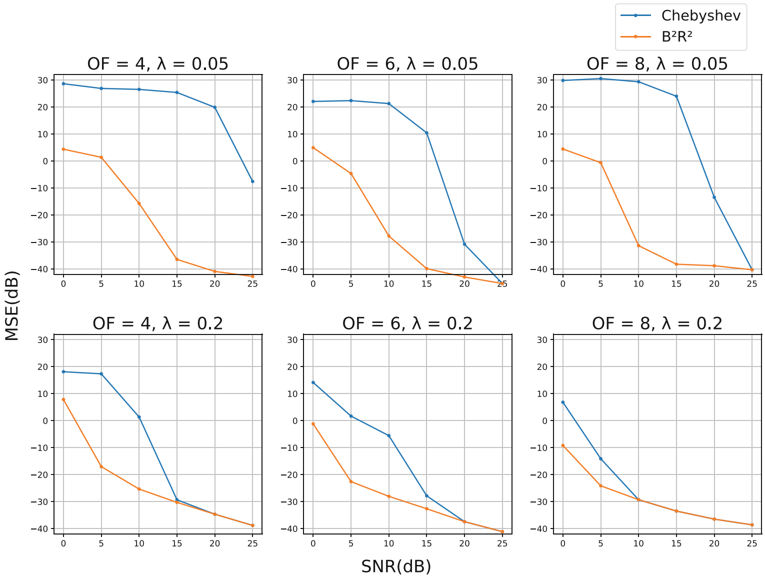

Fig. 9 Comparison of B^2R^2 and Chebyshev algorithms in terms of MSE in recovering a bandlimited signal from modulo samples with OF = 4, 6, 8, and λ = 0.05, 0.2 (cf. [22])

sampling. In this case, the filtered signal will be a bandlimited signal. Then, as with the SoS kernel, one can compute the Fourier samples of the FRI signal from the filtered bandlimited signal by applying DTFT at the desired frequencies [40]. The FRI parameters are estimated from the Fourier samples by applying HRSE approaches. In the modulo framework, the sampling is performed after the modulo operation. Hence, unfolding is to be applied before computing the DTFT. Any one of the approaches discussed in the previous section can be applied for unfolding. A drawback in the lowpass-kernel-based approaches is that the support of the filter is infinite and a countably infinite number of modulo samples are measured to determine the finite number of FRI parameters. It can be shown that for periodic FRI signals, a finite number of time samples measured through a lowpass kernel are sufficient for perfect reconstruction. Precisely, for a L-th degree periodic FRI signal, its $2L$ consecutive Fourier samples can be measured from $2L$ consecutive lowpass-filtered signal samples. Hence, for the reconstruction of FRI signals with modulo samples, it is required to design a local unfolding method that takes a finite number of folded bandlimited samples and estimates $2L$ or more consecutive unfold samples.

Bhandari et al. [38] proposed such a local reconstruction method for FRI signals as well as other parametric signals that can be reconstructed from a finite number of samples [37]. Consider a bandlimited signal $f(t) \in \mathcal{B}_\Omega$ with $\|f\|_\infty \leq \beta_f$. Consider K consecutive modulo samples $\{f_\lambda(nT_s)\}_{n=1}^{K}$. Then a sufficient condition for recovery K' contiguous samples $f(t)$ (up to additive multiples of 2λ) is that

$$T_s \leq \frac{1}{2\Omega e} \quad \text{and} \quad K \geq K' + 7\frac{\beta_f}{\lambda}. \tag{38}$$

In the case of L-th order FRI signal, by choosing $K' \geq 2L$, perfect reconstruction from modulo samples is guaranteed.

The local reconstruction algorithm [38] uses HoD for unfolding and suffers from issues of a high sampling rate and low noise robustness. To address these issues, recovery methods in the Fourier domain have also been explored [20]. Such methods not only offer robustness in the case of system noise [89] and non-ideal folds but also allow for reconstruction at lower sampling rates than what is dictated by the inequality $T_s \leq \frac{1}{2\Omega e}$ for HoD approach.

The proposed Fourier-domain approach considered a K-th order TP signal:

$$f(t) = \sum_{k=-K}^{K} c_k\, e^{\mathrm{j}k\omega_0 t}, \tag{39}$$

where $\omega_0 = \frac{2\pi}{T_0}$ is the fundamental frequency (in rad/s), T_0 is fundamental time period, and K is order of the TP. The coefficients c_ks have Hermitian symmetry, that is, $c^*_{-k} = c_k$, which makes $f(t)$ a real-valued function. A L-th order FRI signal can be equivalently represented as a K-th order TP by using an SoS sampling kernel [16, 62] provided that $K \geq L$. Specifically, for $K \geq L$ all the information of the FRI signal which is required for its reconstruction is retained in the TP (see Sect. 2.3). Hence, modulo sampling and recovery results for a K-th order TP can be extended to FRI signals by using an appropriate sampling kernel. Next, we discuss unfolding of modulo samples of TP signal by using its Fourier-domain properties.

By uniformly sampling $f(t)$ over $(0, T_0]$ using a sampling rate $1/T_s$ results in $P = \lfloor T_0/T_s \rfloor$ samples in a time period. The TP signal can be perfectly reconstructed by determining coefficients c_ks from the unfolded samples provided that $P \geq 2K + 1$. Hence, in the modulo framework, it is sufficient to unfold $P \geq 2K + 1$ uniform samples measured over a time period for perfect reconstruction. In [20], Fourier-domain separation property is used to estimate the residual signal by oversampling. To understand the approach, let us first note that for $T_s = T_0/P$ with $P > 2K + 1$, the DTFT samples of $f(t)$ are given as

$$F(e^{\mathrm{j}m\omega_0 T_s}) = \begin{cases} c_k, & 0 \leq m \leq K, \\ c_{P+k}, & P - K \leq m \leq P - 1, \\ 0, & K + 1 \leq m \leq P - K - 1. \end{cases} \tag{40}$$

The zeros in the DTFT are results of the bandlimited nature of the signal. Next, by using the modulo decomposition as in (27) and (40), the DTFT samples of $f_\lambda(nT_s)$ are given as

$$F_\lambda(e^{\mathrm{j}m\omega_0 T_s}) = Z(e^{\mathrm{j}m\omega_0 T_s}), \quad \text{for} \quad K + 1 \leq m \leq P - K - 1. \tag{41}$$

Hence, one can determine Fourier measurements of the residual signal from that of the modulo samples. To determine $z(nT_s)$ from its partial DTFT samples, FRI nature of $z(t)$ is used. Specifically, for TP signals, $z(t)$ is also periodic and the number of foldings Q is finite (cf. (26)). Hence, its parameters $\{d_m, \tau_m\}_{m=1}^{M}$ can be estimated by applying HRSE approaches such as Prony's method [64] and more to its Fourier samples provided that $P \geq Q+2K+1$. This method is termed as Fourier-Prony approach. From the estimated $z(nT_s)$, unfolded samples can be computed by using (27). The condition $P \geq Q + 2K + 1$ implies that the sampling rate should be greater than or equal to $\frac{Q+2K+1}{T_0}$ for unfolding and reconstruction of K-th order TP. Extending these results to FRI signals, it is inferred that to recover L-th order FRI signal by using an SoS kernel and modulo ADC, it is sufficient to sample at a rate greater than or equal to $\frac{Q+2L+1}{T_0}$. Note that the theoretical minimum sampling rate or rate of innovation is $\frac{2L+1}{T_0}$ and the oversampling is required for unfolding.

The Fourier domain approach allows handling *non-ideal* modulo nonlinearity. To elaborate, consider the functioning of a conventional modulo system where a step function of amplitude 2λ is subtracted when the analog signal crosses the threshold λ. In practice, due to its non-ideal nature, the modulo system may not generate the step function of amplitude 2λ. In such scenarios, the residual signal can still be modeled as in (26) but $d_q \notin 2\lambda\mathbb{Z}$. Even for such a case, the Fourier-Prony method works as it does not depend on the amplitude values of $z(t)$. Hence Fourier-Prony method is immune to such non-ideal acquisitions. There could be other forms of non-idealities in modulo sampling, such as hysteresis, folding transients, etc., and they can be handled by suitably modifying the algorithms [25, 27, 90].

3.4 Modulo Sampling Hardware

We now discuss a couple of hardware prototypes of modulo ADCs. The `US-ADC` was presented in [20]. The electronic circuit, shown in Fig. 10, transforms a continuous-time input signal into a continuous-time modulo signal that can be sampled and digitized later on in the pipeline. An application of the hardware is shown in Fig. 11 where an FRI signal is estimated from its modulo samples [39].

Another modulo hardware prototype is demonstrated in [91, 92]. In the demonstration, the authors presented a high-dynamic-range and wide bandwidth ADC and showed reconstruction of bandlimited signals and FRI signals by using the ADC. Using the hardware board (shown in Fig. 12), it is shown that the FRI signals can be recovered by sampling at 33 times below the Nyquist rate even when the dynamic range of the signal is two to three times higher than that of the ADCs. The FRI signals are filtered using a lowpass kernel prior to sampling. By using a low-rate, robust algorithm [22], it is shown that an FRI signal can be reconstructed up to a 5 dB signal to noise ratio. Further, it is shown that the proposed hardware can sample and recover bandlimited signals from their modulo samples by using the

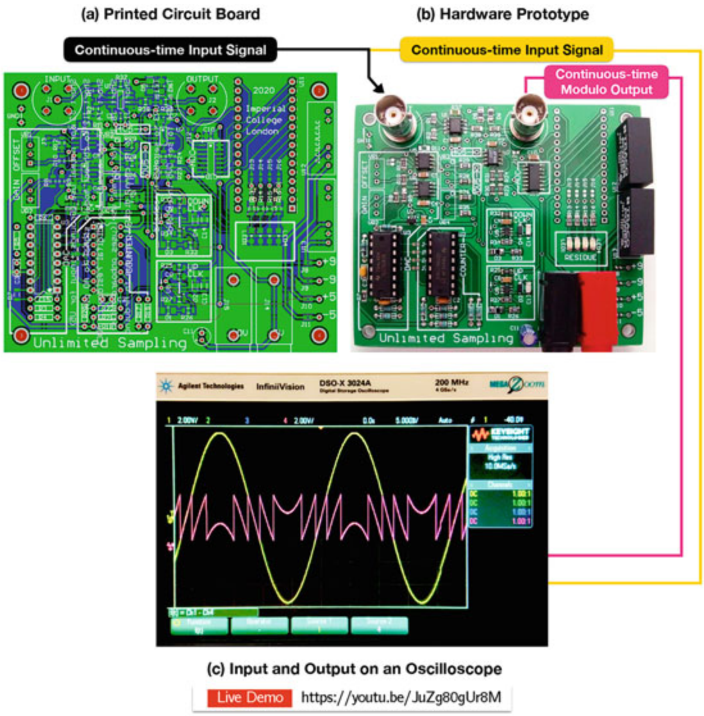

Fig. 10 Modulo ADC Hardware prototype for the Unlimited Sensing Framework. The hardware is capable of folding a signal as large as 24 times the modulo threshold λ. (**a**) Printed circuit board. (**b**) Assembled electronic circuit. The hardware transforms a continuous-time input signal into continuous-time modulo output. (**c**) An oscilloscope screenshot showing the conventional ADC output (yellow) and the Modulo ADC output (pink). Behind the dynamic range of the oscilloscope's built-in ADC, its output measurements are saturated. A YouTube demonstration is available at: https://www.youtube.com/watch?v=JuZg80gUr8M

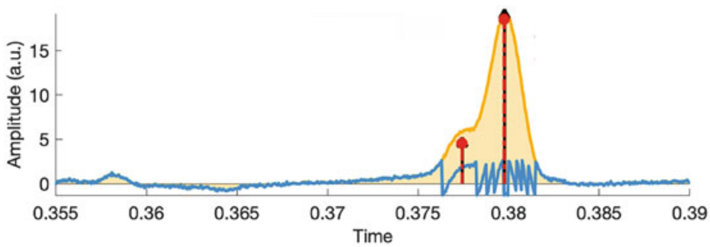

Fig. 11 Hardware experiment for FRI signal recovery: An FRI signal consisting of two spikes is lowpass filtered. The filtered signal (shown in yellow) is sampled by modulo ADC hardware (shown in blue). The spikes estimated directly from the unfolded samples (in black) and estimated via modulo samples (in red) are almost identical (See [39] for details)

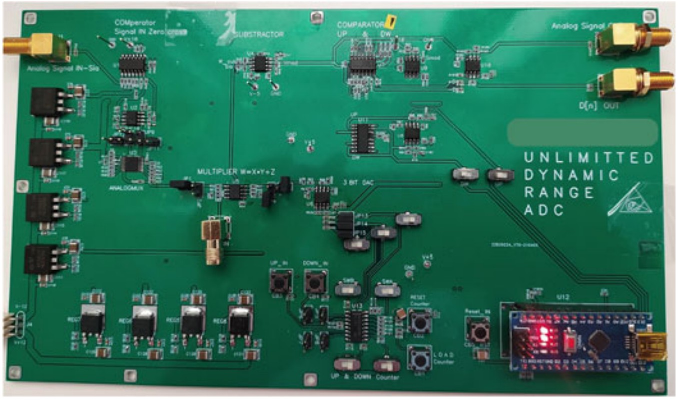

Fig. 12 Hardware board of high dynamic range, wide bandwidth ADC [91, 92]. For further details refer to the webpage: https://www.weizmann.ac.il/math/yonina/software-hardware/hardware

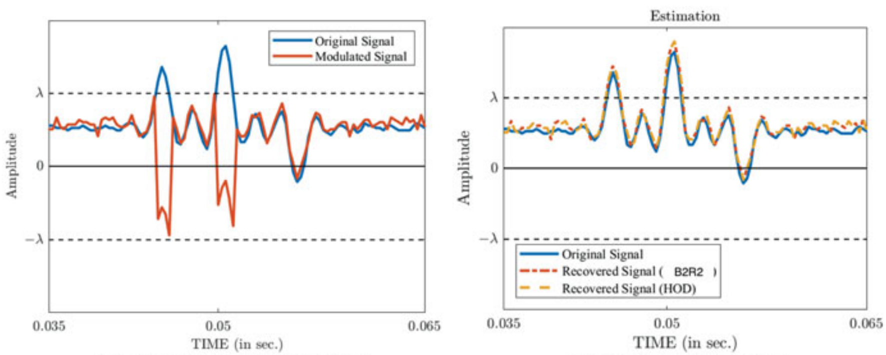

(a) Conventional sampling (b) Modulo sampling

Fig. 13 Hardware experiment for bandlimited signal: A bandlimited signal of 1 kHz is sampled using the hardware shown in Fig. 12. (**a**) Shows the true and folded signal; (**b**) shows the reconstruction by using HoD method (sampling rate 34 kHz) and B^2R^2 algorithm (sampling rate 6 kHz) [92]

B^2R^2 algorithm [22] with a sampling rate three times above the Nyquist rate (see Fig. 13).

4 Task-Based Sampling

In the previous sections, the focus is on different sampling frameworks with the goal of reconstructing analog signals from their discrete representations. A key step that is missing is the quantization of the discrete representations. In practice, an ADC first samples an analog received signal and quantizes it. The desired information is then extracted from these digital representations. Typically, the sampling rate of the conventional ADCs is kept above the Nyquist rate for bandlimited signals (or above the rate of innovation for FRI signals), and high-resolution quantization is used for close-to-perfect recovery. The large number of measurements generated at a high sampling rate and a large number of bits used in high-resolution quantizers result in high-power ADCs. In addition, in multi-receiver systems, analog signals are captured through multiple sensors. In such systems, each receiver has its own ADC, and hence overall power consumption is proportional to the number of ADCs. For example, in beyond 5G wireless communication systems, massive multiple-input multiple-output (MIMO) antenna systems are being used together with large bandwidths in the millimeter-wave (mmWave) bands [93]. Such systems with conventional ADCs would be inefficient since the power consumption and memory requirements increase with the sampling rate and the number of signals to be sampled. In addition, each signal component is sampled using a separate ADC and then quantized individually, which increases the power and cost of the overall system.

In many applications, the goal or task is to extract some underlying information from the digital samples rather than signal reconstruction. Since the information is embedded in a lower dimension compared to the ambient dimension of the samples, the samples can be combined before extracting the necessary information. Similarly, in a multi-receiver system, the analog signals from multiple sensors can be combined by using an analog combiner prior to sampling [28, 29]. Then the signals are sampled and quantized in the reduced dimension. This results in a smaller number ADCs and hence lower power requirements. Further, assuming that the total number of quantization bits is fixed and finite, a higher number of bits can be assigned to each sample in the reduced dimension space compared to that in the original signal dimension [28, 29]. Hence, the mentioned hardware-limited framework resolution can be improved without increasing the memory requirement. In the following, we introduce hardware-limited task-based quantization systems and discuss systems with linear and quadratic tasks.

4.1 Theory of Task-Based Quantizers

In this section, we introduce a general discrete model of the hardware-limited task-based quantization system [28]. In this discrete model, the sampling part is ignored, and only quantization aspects of the ADC are considered. A task-based ADC with sampling and quantization is discussed in [29]. Since the signals are in the discrete domain, we denote them by vectors. A schematic of the discrete system is shown in Fig. 14 where the goal is to recover the information vector $\mathbf{s} \in \mathbb{R}^k$, which is statistically related to observed signal $\mathbf{x} \in \mathbb{R}^n$. The information vector $\mathbf{s}$ and the observed signal $\mathbf{x}$ are statistically related with function $f_{\mathbf{x}|\mathbf{s}}$ and $k < n$. The model represents a broad range of applications, such as time-of-flight imaging [94], where

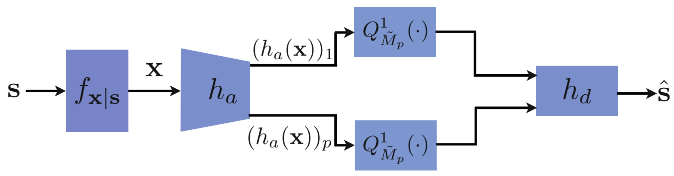

Fig. 14 A schematic of hardware-limited task-based quantizer [28]

$\mathbf{s}$ represents the time delays and amplitudes of the pulses and $\mathbf{x}$ denotes the observed signal.

To estimate $\mathbf{s}$, $\mathbf{x}$ is first projected to a lower-dimensional space $\mathcal{R}^p$, $p \leq n$, by using an analog combiner $h_a(\cdot)$. The low-dimensional signal is then quantized as detailed next. Let M denote the overall number of quantization levels, which represents the memory requirement of the system. Then, each component of $h_a(\mathbf{x})$ is quantized with resolution $\tilde{M}_p \triangleq \lfloor M^{1/p} \rfloor$, whose operation is denoted as $Q^1_{\tilde{M}_p}(\cdot)$. In $Q^1_{\tilde{M}_p}(\cdot)$, the superscript one signifies that it is a scalar quantizer. Different choices of p will result in different levels of quantizations as M is fixed and $(\tilde{M}_p)^p \leq M$. After quantization, as estimate of $\mathbf{s}$, is estimated by the post-quantization processing module $h_d(\cdot) : \mathcal{R}^p \longmapsto \mathcal{R}^k$. The estimate is given as

$$\hat{\mathbf{s}} = h_d\left(Q^1_{\tilde{M}_p}\left((h_a(\mathbf{x}))_1\right), \cdots, Q^1_{\tilde{M}_p}\left((h_a(\mathbf{x}))_p\right)\right). \tag{42}$$

Due to quantization, the estimator $\hat{\mathbf{s}}$ is also denoted as a quantized representation of $\mathbf{s}$. Task-based quantization has been explored in [95, 96] but without any dimensionality reduction. While preserving the required information about $\mathbf{s}$ even after low-bit simple scalar quantization, the combiners also facilitate low-cost hardware implementation by reducing the number of radiofrequency (RF) chains.

The problem in hardware-limited task-based quantization is to jointly design the analog combiner $h_a(\cdot)$, the quantization rule of $Q^1_{\tilde{M}_p}(\cdot)$, and the digital processing part $h_d(\cdot)$ according to an appropriate metric. However, explicitly characterizing the general quantization system is difficult. Therefore, [28] and [30] focus on scenarios in which the stochastic relationship $f_{\mathbf{x}|\mathbf{s}}$ is linear or quadratic, as discussed in the following subsections.

4.2 Linear Estimation Tasks

In this framework, we consider scenarios in which the stochastic relationship between the task vector $\mathbf{s}$ and the observations $\mathbf{x}$ is linear. Such a relationship exists, for example, in the channel estimation problem of wireless communications systems, where the task vector $\mathbf{s}$ represents the unknown channel. By defining the pilot matrix as $\mathbf{D}$, the received signal can be expressed as $\mathbf{x} = \mathbf{D}\mathbf{s} + \mathbf{w}$, with $\mathbf{w}$ as the additive noise term.

In this case, the optimal linear estimation of $\mathbf{s}$ from $\mathbf{x}$ is given by $\tilde{\mathbf{s}} = \boldsymbol{\Gamma}\mathbf{x}$, where $\boldsymbol{\Gamma}$ is the linear minimum mean square error (MMSE) estimation matrix. Since the model and MMSE estimator are linear, the analog combiner and the digital processing module are set to be linear: $h_a(\mathbf{x}) = \mathbf{A}\mathbf{x}$, $\mathbf{A} \in \mathbb{R}^{p\times n}$, and $h_d(\mathbf{u}) = \mathbf{B}\mathbf{u}$, $\mathbf{B} \in \mathbb{R}^{k\times p}$. Furthermore, dithered quantization model [97] is assumed to mathematically characterize the input-output relationship of the quantizer $Q^1_{\tilde{M}_p}(\cdot)$. In this model, the quantizer's output can be written as a sum of the input and a white noise term, provided that the input is inside the dynamic range of the quantizer. Hence, the overall structure of the system shown in Fig. 14 is linear.

The accuracy of the estimation is measured in terms of mean-squared error (MSE) $E[||\mathbf{s} - \hat{\mathbf{s}}||^2]$ which can be decomposed by using the orthogonality principle as

$$E[||\mathbf{s} - \hat{\mathbf{s}}||^2] = E[||\mathbf{s} - \tilde{\mathbf{s}}||^2] + E[||\tilde{\mathbf{s}} - \hat{\mathbf{s}}||^2]. \tag{43}$$

In the decomposition, the first term is the error of the MMSE estimate, and the *second term* is the distortion with respect to the MMSE estimate. Since the first term does not depend on $\hat{\mathbf{s}}$, we refer to the second term as MSE distortion.

Let $\boldsymbol{\Sigma}_{\mathbf{x}}$ be the covariance matrix of observations $\mathbf{x}$, γ the dynamic range of the scalar quantizers, z_l, $l = 1, \ldots, p$ the dither signals, and $\mathbf{A}^\circ$ and $\mathbf{B}^\circ$, respectively, the optimal analog and digital processing matrices that achieve the minimal MSE distortion. Then the following results are presented in [28]:

Theorem 5 *For any analog combining matrix $\mathbf{A}$ and dynamic range γ such that $Pr(|(\mathbf{A}\mathbf{x})_l + z_l| > \gamma) = 0$, namely, the quantizers operate within their dynamic range with probability one, the digital processing matrix which minimizes the MSE is given by*

$$\mathbf{B}^\circ(\mathbf{A}) = \boldsymbol{\Gamma}\boldsymbol{\Sigma}_{\mathbf{x}}\mathbf{A}^T\left(\mathbf{A}\boldsymbol{\Sigma}_{\mathbf{x}}\mathbf{A}^T + \frac{2\gamma^2}{3\tilde{M}_p^2}\mathbf{I}_p\right)^{-1}. \tag{44}$$

Theorem 6 *For the hardware-limited quantization system based on the model depicted in Fig. 14, the analog combining matrix $\mathbf{A}^\circ$ is given by $\mathbf{A}^\circ = \mathbf{U}_{\mathbf{A}}\boldsymbol{\Lambda}_{\mathbf{A}}\mathbf{V}_{\mathbf{A}}^T\boldsymbol{\Sigma}_{\mathbf{x}}^{-1/2}$, where*

- *$\mathbf{V}_{\mathbf{A}} \in \mathcal{R}^{n\times n}$ is the right singular vectors matrix of $\tilde{\boldsymbol{\Gamma}} \triangleq \boldsymbol{\Gamma}\boldsymbol{\Sigma}_{\mathbf{x}}^{1/2}$.*
- *$\boldsymbol{\Lambda}_{\mathbf{A}} \in \mathcal{R}^{p\times n}$ is a diagonal matrix with diagonal entries*

$$(\boldsymbol{\Lambda}_{\mathbf{A}})^2_{i,i} = \frac{2\kappa_p}{3\tilde{M}_p^2\cdot p}\left(\zeta\cdot\lambda_{\tilde{\boldsymbol{\Gamma}},i} - 1\right)^+,$$

where $\kappa_p = \eta^2 \left(1 - \frac{\eta^2}{3\tilde{M}_p^2}\right)^{-1}$ *with* η *denoting a constant that is set to guarantee that the quantizer operates within the dynamic range [28],* $\{\lambda_{\tilde{\mathbf{\Gamma}},i}\}$ *are singular values of* $\tilde{\mathbf{\Gamma}}$ *arranged in a descending order, and* ζ *is chosen such that*

$$\frac{2\kappa_p}{3\tilde{M}_p^2 \cdot p} \sum_{i=1}^{p} \left(\zeta \cdot \lambda_{\tilde{\mathbf{\Gamma}},i} - 1\right)^+ = 1.$$

- $\mathbf{U_A} \in \mathcal{R}^{p \times p}$ *is a unitary matrix which guarantees that* $\mathbf{U_A \Lambda_A \Lambda_A^T U_A^T}$ *has identical diagonal entries.*

The dynamic range of the quantizer is given by

$$\gamma^2 = \frac{\eta^2}{p}\left(1 - \frac{\eta^2}{3\tilde{M}_p^2}\right)^{-1}, \tag{45}$$

and the resulting minimal achievable distortion is

$$E[||\tilde{\mathbf{s}} - \hat{\mathbf{s}}||^2] = \begin{cases} \sum_{i=1}^{k} \frac{\lambda_{\tilde{\mathbf{\Gamma}},i}^2}{\left(\zeta \cdot \lambda_{\tilde{\mathbf{\Gamma}},i} - 1\right)^+ + 1}, & p \geq k, \\ \sum_{i=1}^{p} \frac{\lambda_{\tilde{\mathbf{\Gamma}},i}^2}{\left(\zeta \cdot \lambda_{\tilde{\mathbf{\Gamma}},i} - 1\right)^+ + 1} + \sum_{i=p+1}^{k} \lambda_{\tilde{\mathbf{\Gamma}},i}^2, & p < k. \end{cases} \tag{46}$$

Following are some insights based on the characterization of the task-based quantization system in Theorem 6 [28]:

(1) In order to minimize the MSE, p must not be larger than the rank of the covariance matrix of the MMSE estimate $\tilde{\mathbf{s}}$. This implies that reducing the dimensionality of the input prior to quantization contributes to recovering the task vector as higher resolution quantizers can be used without violating the overall bit constraint; and
(2) when the covariance matrix of $\tilde{\mathbf{s}}$ is non-singular, quantizing the MMSE estimate minimizes the MSE if and only if the covariance matrix of $\tilde{\mathbf{s}}$ equals $\mathbf{I}_k$ up to a constant factor. This indicates that, except for very specific models, quantizing the entries of the MMSE estimate vector, which is the optimal strategy when using vector quantizers [98], does not minimize the MSE when using uniform scalar ADCs.

4.3 Quadratic Estimation Tasks

In this section, we consider a model where the task-vector $\mathbf{s}$ is a quadratic function of the observation vector $\mathbf{x}$. Such scenarios arise in the covariance estimation problem [99] and in the problem of direction of arrival (DOA) estimation from autocorrelation matrix [100]. To model the quadratic task, we assume that $\mathbf{x} \in \mathcal{R}^n$ follows a Gaussian distribution. The task is to recover a set of quadratic functions $\{\mathbf{x}^T \mathbf{C}_i \mathbf{x}\}_{i=1}^k$, where each $\mathbf{C}_i \in \mathcal{R}^{n\times n}$ satisfies $E[\mathbf{x}^T \mathbf{C}_i \mathbf{x}] < \infty$. In the covariance estimation problem, we have $k = 1$ and $\mathbf{C}_1$ is an identity matrix.

The quadratic functions $\{\mathbf{x}^T \mathbf{C}_i \mathbf{x}\}_{i=1}^k$ form the elements of the task vectors as $(\mathbf{s})_i \triangleq \mathbf{x}^T \mathbf{C}_i \mathbf{x}$. The task vector can be written as $\mathbf{s} = \mathbf{G}\underline{\mathbf{x}}$ where $\underline{\mathbf{x}} \triangleq \mathrm{vec}(\mathbf{x}\mathbf{x}^T)$ and the matrix $\mathbf{G} \in \mathcal{R}^{k\times n^2}$ whose ith row is given by $\mathrm{vec}^T(\mathbf{C}_i)$. In this representation, the task vector is a linear combination of the $\underline{\mathbf{x}}$, and hence linear task-based quantization framework described in the previous is applicable. Under the constraint that the overall number of quantization levels, M, is fixed, the achievable MSE is given in the following theorem [30, 101]:

Theorem 7 *For any analog combining matrix* $\mathbf{A}$ *and dynamic range* γ *such that* $Pr\big(|(\mathbf{A}\underline{\mathbf{x}})_l + z_l| > \gamma\big) = 0$, *namely, the quantizers operate within their dynamic range with probability one, the following MSE is achievable:*

$$MSE(\mathbf{A}) = Tr\left(\mathbf{G}\boldsymbol{\Sigma}_{\underline{\mathbf{x}}}\mathbf{G}^T - \mathbf{G}\boldsymbol{\Sigma}_{\underline{\mathbf{x}}}\mathbf{A}^T\left(\mathbf{A}\boldsymbol{\Sigma}_{\underline{\mathbf{x}}}\mathbf{A}^T + \frac{2\gamma^2}{3\tilde{M}_p^2}\mathbf{I}_p\right)^{-1}\mathbf{A}\boldsymbol{\Sigma}_{\underline{\mathbf{x}}}\mathbf{G}^T\right). \tag{47}$$

where $\boldsymbol{\Sigma}_{\underline{\mathbf{x}}}$ *denotes the covariance matrix of* $\underline{\mathbf{x}}$.

The minimum MSE is achievable by setting the digital matrix $\mathbf{B}$ *as*

$$\mathbf{B} = \mathbf{G}\boldsymbol{\Sigma}_{\underline{\mathbf{x}}}\mathbf{A}^T\left(\mathbf{A}\boldsymbol{\Sigma}_{\underline{\mathbf{x}}}\mathbf{A}^T + \frac{2\gamma^2}{3\tilde{M}_p^2}\mathbf{I}_p\right)^{-1}, \tag{48}$$

and the analog matrix $\mathbf{A}$ *as* $\mathbf{A} = \mathbf{U}_{\mathbf{A}}\boldsymbol{\Lambda}_{\mathbf{A}}\mathbf{V}_{\mathbf{A}}^T\boldsymbol{\Sigma}_{\underline{\mathbf{x}}}^{-1/2}$, *where*

- $\mathbf{V}_{\mathbf{A}} \in \mathcal{R}^{n^2\times n^2}$ *is the right singular vectors matrix of* $\tilde{\mathbf{G}} \triangleq \mathbf{G}\boldsymbol{\Sigma}_{\underline{\mathbf{x}}}^{1/2}$.
- $\boldsymbol{\Lambda}_{\mathbf{A}} \in \mathcal{R}^{p\times n^2}$ *is a diagonal matrix with diagonal entries*

$$(\boldsymbol{\Lambda}_{\mathbf{A}})_{i,i}^2 = \frac{2\kappa_p}{3\tilde{M}_p^2\cdot p}\left(\zeta\cdot\lambda_{\tilde{\mathbf{G}},i} - 1\right)^+,$$

where $\kappa_p = \eta^2\left(1 - \frac{\eta^2}{3\tilde{M}_p^2}\right)^{-1}$ *with* η *denoting a constant that is set to guarantee that the quantizer operates within the dynamic range [30],* $\{\lambda_{\tilde{\mathbf{G}},i}\}$ *are singular values of* $\tilde{\mathbf{G}}$ *arranged in descending order, and* ζ *is set such that*

$$\frac{2\kappa_p}{3\tilde{M}_p^2\cdot p}\sum_{i=1}^{p}\left(\zeta\cdot\lambda_{\tilde{\mathbf{G}},i} - 1\right)^+ = 1.$$

- $\mathbf{U_A} \in \mathcal{R}^{p \times p}$ *is a unitary matrix which guarantees that* $\mathbf{U_A \Lambda_A \Lambda_A^T U_A^T}$ *has identical diagonal entries.*

The above discussion shows that by properly organizing the observations, quadratic tasks can be solved by applying a linear task-based quantization framework, and dimensionality can be reduced from n^2 to p. Hence, under fixed bits constraint, more bits are allowed and thus higher resolution for each channel compared with the task-ignorant scheme.

To evaluate the performance of the task-based system, covariance recovery problem is considered [28, 30]. In this scenario, the following quantizers are evaluated in Fig. 15 in terms of the achievable MSE versus the number of bits [30]:

1. The quadratic task-based quantization system is presented in the subsection with $p = 6$.
2. The linear quantization system.
3. A task ignorant system which quantizes $\mathbf{x}$ and computes the empirical covariance at the output of the ADC.
4. A system which recovers $\mathbf{s}$ in analog and set $\hat{\mathbf{s}}$ to be the output of the ADC.

From Fig. 15, we note that the quadratic task-based quantizer has the lowest MSE. While quantizing $\mathbf{s}$ directly results in notable quantization errors when operating with a small number of bits, due to the need to set the dynamic range to a relatively large value resulting in coarse quantization. The error of the task-ignorant quantization and the linear combining ones are comparatively high, even with large quantization bits.

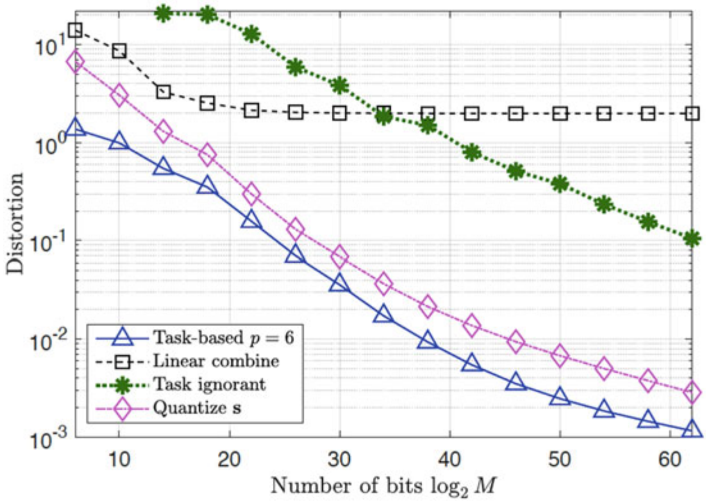

Fig. 15 Distortions of empirical covariance recovery versus number of bits [30]

In the scenarios where $f_{\mathbf{x}|\mathbf{s}}$ is too complex to be represented either linearly/quadratically or accurate knowledge of the statistical relationship is not available, a data-driven deep-learning approach can be applied [31]. The proposed deep task-based quantization scheme learns the analog and digital processing parts, parameterized as layers of deep neural networks (DNNs), and the scalar quantizer, which is modeled as an activation function between two intermediate layers in an end-to-end manner from a set of training data. With such a system architecture, tasks including estimation and classification can be performed by, respectively, setting the loss functions as empirical MSE and cross-entropy (see [31] for details). In addition to the theoretical results, the performance of the hardware-limited task-based quantization systems is also evaluated for applications such as finite intersymbol interference (ISI) channel estimation and covariance recovery [28, 30]. In both the applications, the task-based quantization can achieve comparable performance with a small number of bits compared with the conventional high-resolution quantization scheme and hence addressing the power consumption and storage issues of conventional ADCs. Further, task-based quantization is applied to massive MIMO communications for estimation of the underlying channel from the high-dimensional received signals [32], target identification in radar [33], graph signal processing [102], and joint radar communications [34]. In all these problems, the analog signals are acquired not with the goal of being reconstructed but for a specific task, and applying task-based quantization together with analog combiners reduces the power consumption and memory requirements.

4.4 Task-Based ADC Hardware

A hardware prototype for MIMO channel reduction with the task of estimating the underlying channel is presented in [35]. In order to reduce the number of receive RF chains, a hardware prototype implementing analog combining for RF chain reduction is demonstrated. The prototype consists of a specially designed configurable combining board as well as a dedicated experimental setup as shown in Fig. 16. The parameters of the combiners are optimized for the channel estimation task. The Kronecker channel model with known second-order statistics of the channel (i.e., transmit and receive side covariance matrices) is adopted, and it is shown that the optimal combiner corresponds to the first eigenvectors of the receive side covariance matrix. Afterwards, the channel estimation with reduced receive RF chains is realized following a Bayesian approach, by applying the minimum mean squared error (MMSE) channel estimator to the output of our proposed analog combiner. In Fig. 17, channel estimation accuracy in terms of MSE is compared for different noise levels. We note that combiners that are optimized for their gains or phase have lower error than a random combination. A hardware prototype was built where the quantization bits are dynamically adjustable [103]. The developed hardware platform is applied to the implementation of channel estimation in massive MIMO systems.

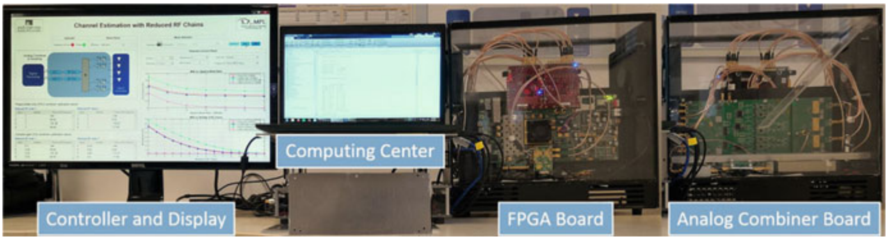

Fig. 16 A hardware prototype of task-aware MIMO RF chain reduction system [35]. For further details refer to the webpage: https://www.weizmann.ac.il/math/yonina/software-hardware/hardware

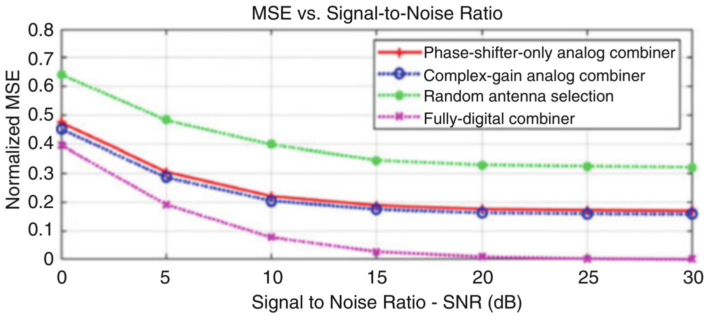

Fig. 17 A comparison of different analog combiners in terms of channel estimation accuracy vs SNR

Recently, a hardware prototype is demonstrated for task-based quantization for multi-user recovery [104]. In this prototype, a configurable quantization hardware is designed, consisting of an analog combiner to reduce the input dimensionality and scalar quantizers with dynamically adjustable quantization bits. The developed hardware platform (see Fig. 18) is then applied to multi-user signal recovery. The demonstration platform consists of a 16×2 analog combiner and a configurable quantizer, including 2, 3, 4 and 12 bits quantization. Using a dedicated GUI, the demo shows that the nearly optimal performance of multi-user signal recovery can be achieved with a low-bit quantizer by accounting for the task.

5 Conclusions

In this chapter, we discussed three ADC frameworks that are based on low-power consumption. First, we discussed IF-TEM as an alternative to conventional sampling. IF-TEM-based ADCs represent analog signals through a set of time instances and do not require a clock. Second, we discussed the dynamic range aspect of ADC and show that by using a modulo operation prior to sampling a low-dynamic

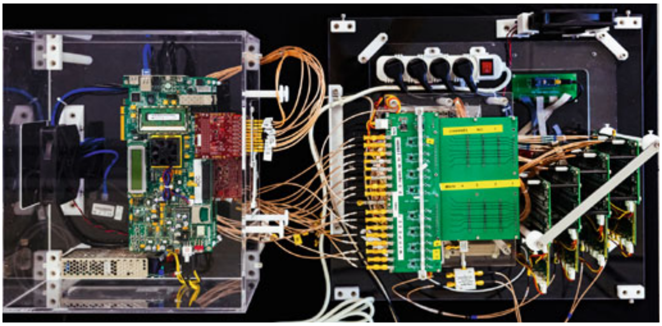

Fig. 18 A hardware prototype board of task-based quantization for multi-user recovery [104]

range, low-power ADC can sample signals beyond its bandwidth. We discussed reconstruction algorithms for bandlimited and FRI signals for IF-TEM and modulo sampling. Third, we introduced hardware-limited task-based quantization, including the general system model and the specific system design for linear and quadratic tasks. By using an analog combiner, the task-based quantization system significantly outperforms its task-ignorant counterpart when the total number of quantization bits is fixed. For all these three frameworks, we discussed hardware prototypes that are developed in our labs. These power-efficient ADCs play a crucial role in designing compact, portable medical and communication devices.

References

1. Y.C. Eldar, *Sampling Theory: Beyond Bandlimited Systems* (Cambridge University Press, 2015)
2. C.E. Shannon, A mathematical theory of communication. Bell Syst. Tech. J. **27**, 623–656 (1948)
3. H. Nyquist, Certain topics in telegraph transmission theory. Trans. Am. Inst. Elect. Eng. **47**(2), 617–644 (1928)
4. J.R. Higgins, Five short stories about the cardinal series. Bull. Am. Math. Soc. **12**(1), 45–89 (1985)
5. A.A. Lazar, L.T. Tóth, Time encoding and perfect recovery of bandlimited signals, in *Proceedings of IEEE International Conference on Acoustics, Speech and Signal Processing (ICASSP)*, vol. 6 (IEEE, 2003), pp. VI–709
6. A.A. Lazar, L.T. Tóth, Perfect recovery and sensitivity analysis of time encoded bandlimited signals. IEEE Trans. Circuits Syst. I: Reg. Pap. **51**(10), 2060–2073 (2004)
7. A.A. Lazar, Time encoding with an integrate-and-fire neuron with a refractory period. Neurocomputing **58**, 53–58 (2004)
8. H. Naaman, S. Mulleti, Y.C. Eldar, FRI-TEM: time encoding sampling of finite-rate-of-innovation signals. IEEE Trans. Signal Process (2022), to appear
9. R. Kumaresan, N. Panchal, Encoding bandpass signals using zero/level crossings: a model-based approach. IEEE Trans. Audio Speech Lang. Process. **18**(1), 17–33 (2010)
10. N. Sayiner, H. Sorensen, T. Viswanathan, A level-crossing sampling scheme for A/D conversion. IEEE Trans. Circuits Syst. II: Analog Digital Signal Process. **43**(4), 335–339 (1996)

11. S. Senay, J. Oh, L.F. Chaparro, Regularized signal reconstruction for level-crossing sampling using Slepian functions. Signal Process. **92**(4), 1157–1165 (2012)
12. K. Guan, A.C. Singer, A level-crossing sampling scheme for non-bandlimited signals, in *Proceedings of IEEE International Conference on Acoustics, Speech and Signal Processing (ICASSP)*, vol. 3 (IEEE, 2006), p. III
13. B.F. Logan Jr, Information in the zero crossings of bandpass signals. Bell Syst. Tech. J. **56**(4), 487–510 (1977)
14. F. Bond, C. Cahn, On the sampling the zeros of bandwidth limited signals. IRE Trans. Info. Theory **4**(3), 110–113 (1958)
15. A. Mamistvalov, Y.C. Eldar, Compressed Fourier-domain convolutional beamforming for sub-Nyquist ultrasound imaging. IEEE Trans. Ultrason. Ferroelectr. Freq. Control **69**(2), 489–499 (2022)
16. R. Tur, Y.C. Eldar, Z. Friedman, Innovation rate sampling of pulse streams with application to ultrasound imaging. IEEE Trans. Signal Process. **59**(4), 1827–1842 (2011)
17. A. Bhandari, F. Krahmer, R. Raskar, On unlimited sampling, in *International Conference on Sampling Theory and Applications (SampTA)*, 2017, pp. 31–35
18. A. Bhandari, F. Krahmer, R. Raskar, On unlimited sampling and reconstruction. IEEE Trans. Signal Process. **69**, 3827–3839 (2020)
19. A. Bhandari, F. Krahmer, R. Raskar, Methods and apparatus for modulo sampling and recovery, US Patent US10 651 865B2, 2020
20. A. Bhandari, F. Krahmer, T. Poskitt, Unlimited sampling from theory to practice: Fourier-Prony recovery and prototype ADC. IEEE Trans. Signal Process. **701**, 1131–1141 (2021)
21. E. Romanov, O. Ordentlich, Above the Nyquist rate, modulo folding does not hurt. IEEE Signal Process. Lett. **26**(8), 1167–1171 (2019)
22. E. Azar, S. Mulleti, Y.C. Eldar, Residual recovery algorithm for modulo sampling, in *IEEE International Conference on Acoustics, Speech and Signal Processing (ICASSP)* (2022)
23. E. Azar, S. Mulleti, Y.C. Eldar, Robust unlimited sampling beyond modulo. IEEE Trans. Signal Process. (2022), submitted
24. D. Florescu, F. Krahmer, A. Bhandari, Event-driven modulo sampling, in *IEEE International Conference on Acoustics, Speech and Signal Processing (ICASSP)*, 2021, pp. 5435–5439
25. D. Florescu, F. Krahmer, A. Bhandari, The surprising benefits of hysteresis in unlimited sampling: theory, algorithms and experiments. IEEE Trans. Signal Process. **70**, 616–630 (2022)
26. M. Beckmann, A. Bhandari, F. Krahmer, The modulo Radon transform: theory, algorithms, and applications. SIAM J. Imag. Sci. **15**(2), 455–490 (2022)
27. D. Florescu, A. Bhandari, Modulo event-driven sampling: System identification and hardware experiments, in *IEEE International Conference on Acoustics, Speech and Signal Processing (ICASSP)*, 2022, pp. 5747–5751
28. N. Shlezinger, Y.C. Eldar, M.R.D. Rodrigues, Hardware-limited task-based quantization. IEEE Trans. Signal Process. **67**(20), 5223–5238 (2019)
29. P. Neuhaus, N. Shlezinger, M. Dörpinghaus, Y.C. Eldar, G. Fettweis, Task-based analog-to-digital converters. IEEE Trans. Signal Process. **69**, 5403–5418 (2021)
30. S. Salamatian, N. Shlezinger, Y.C. Eldar, M. Médard, Task-based quantization for recovering quadratic functions using principal inertia components, in *Proceedings, IEEE ISIT*, Paris, 2019, pp. 390–394
31. N. Shlezinger, Y.C. Eldar, Deep task-based quantization. Entropy **23**(104), 1–18 (2021)
32. N. Shlezinger, Y.C. Eldar, M.R.D. Rodrigues, Asymptotic task-based quantization with application to massive MIMO. IEEE Trans. Signal Process. **67**(15), 3995–4012 (2019)
33. F. Xi, N. Shlezinger, Y.C. Eldar, BiLiMO: Bit-limited MIMO radar via task-based quantization. IEEE Trans. Signal Process., to appear
34. D. Ma, N. Shlezinger, T. Huang, Y. Liu, Y.C. Eldar, Bit constrained communication receivers in joint radar communications systems, in *Proceedings, IEEE ICASSP*, Toronto, 2021, pp. 8243–8247
35. T. Gong, N. Shlezinger, S.S. Ioushua, M. Namer, Z. Yang, Y.C. Eldar, RF chain reduction for MIMO systems: a hardware prototype. IEEE Syst. J. **14**(4), 5296–5307 (2020)

36. A. Bhandari, F. Krahmer, HDR imaging from quantization noise, in *IEEE International Conference on Image Processing (ICIP)*, 2020, pp. 101–105
37. A. Bhandari, F. Krahmer, R. Raskar, Unlimited sampling of sparse sinusoidal mixtures, in *IEEE International Symposium on Information Theory (ISIT)*, 2018, pp. 336–340
38. A. Bhandari, F. Krahmer, R. Raskar, Unlimited sampling of sparse signals, in *IEEE International Conference on Acoustics, Speech and Signal Processing (ICASSP)*, 2018, pp. 4569–4573
39. A. Bhandari, Back in the US-SR: unlimited sampling and sparse super-resolution with its hardware validation. IEEE Signal Process. Lett. **29**, 1047–1051 (2022)
40. M. Vetterli, P. Marziliano, T. Blu, Sampling signals with finite rate of innovation. IEEE Trans. Signal Process. **50**(6), 1417–1428 (2002)
41. T. Blu, P.-L. Dragotti, M. Vetterli, P. Marziliano, L. Coulot, Sparse sampling of signal innovations. IEEE Signal Process. Mag. **25**(2), 31–40 (2008)
42. F. Marvasti, *Nonuniform Sampling: Theory and Practice*. Information Technology Series (Springer, 2001)
43. Y.C. Eldar, A.V. Oppenheim, Filterbank reconstruction of bandlimited signals from nonuniform and generalized samples. IEEE Trans. Signal Process. **48**(10), 2864–2875 (2000)
44. E. Margolis, Y.C. Eldar, Nonuniform sampling of periodic bandlimited signals. IEEE Trans. Signal Process. **56**(7), 2728–2745 (2008)
45. K. Yao, J. Thomas, On some stability and interpolatory properties of nonuniform sampling expansions. IEEE Trans. Circuit Theory **14**(4), 404–408 (1967)
46. H.G. Feichtinger, J.C. Príncipe, J.L. Romero, A. Singh Alvarado, G.A. Velasco, Approximate reconstruction of bandlimited functions for the integrate and fire sampler. Adv. Comput. Math. **36**(1), 67–78 (2012)
47. J. Yen, On nonuniform sampling of bandwidth-limited signals. IRE Trans. Circuit Theory **3**(4), 251–257 (1956)
48. R.F. Bass, K. Gröchenig, Random sampling of bandlimited functions. Israel J. Math. **177**(1), 1–28 (2010)
49. D.M. Klamer, E. Masry, Polynomial interpolation of randomly sampled bandlimited functions and processes. SIAM J. Appl. Math. **42**(5), 1004–1019 (1982)
50. M. Malmirchegini, M.M. Kafashan, M. Ghassemian, F. Marvasti, Non-uniform sampling based on an adaptive level-crossing scheme. IET Signal Process. **9**, 484–490(6) (2015)
51. J.J. Benedetto, *Wavelets: Mathematics and Applications* (CRC Press, 2021)
52. H. Naaman, S. Mulleti, Y.C. Eldar, Integrate and fire circuit as an ADC replacement, in *IEEE International Symposium Information Theory (ISIT)*, 2022
53. S. Rudresh, A.J. Kamath, C.S. Seelamantula, A time-based sampling framework for finite-rate-of-innovation signals, in *Proceedings of IEEE International Conference on Acoustics, Speech and Signal Processing (ICASSP)*, 2020, pp. 5585–5589
54. H.G. Feichtinger, K. Gröchenig, Iterative reconstruction of multivariate bandlimited functions from irregular sampling values. SIAM J. Math. Anal. **23**(1), 244–261 (1992)
55. K. Adam, A. Scholefield, M. Vetterli, Encoding and decoding mixed bandlimited signals using spiking integrate-and-fire neurons, in *Proceedings of IEEE International Conference on Acoustics, Speech and Signal Processing (ICASSP)*, 2020, pp. 9264–9268
56. K. Adam, A. Scholefield, M. Vetterli, Sampling and reconstruction of bandlimited signals with multi-channel time encoding. IEEE Trans. Signal Process. **68**, 1105–1119 (2020)
57. A.A. Lazar, E.A. Pnevmatikakis, Faithful representation of stimuli with a population of integrate-and-fire neurons. Neural Comput. **20**(11), 2715–2744 (2008)
58. D. Gontier, M. Vetterli, Sampling based on timing: time encoding machines on shift-invariant subspaces. Appl. Comput. Harmonic Anal. **36**(1), 63–78 (2014)
59. Y.C. Eldar, *Sampling Theory: Beyond Bandlimited Systems* (Cambridge University Press, 2015)
60. M. Mishali, Y.C. Eldar, From theory to practice: Sub-Nyquist sampling of sparse wideband analog signals. IEEE J. Sel. Top. Signal Process. **4**(2), 375–391 (2010)
61. M. Mishali, Y.C. Eldar, Sub-Nyquist sampling. IEEE Signal Process. Mag. **28**(6), 98–124 (2011)

62. S. Mulleti, C.S. Seelamantula, Paley-Wiener characterization of kernels for finite-rate-of-innovation sampling. IEEE Trans. Signal Process. **65**(22), 5860–5872 (2017)
63. P. Stoica, R.L. Moses, *Introduction to Spectral Analysis* (Prentice Hall, Upper Saddle River, 1997)
64. G.R. DeProny, Essai experimental et analytique: Sur les lois de la dilatabilité de fluides élastiques et sur celles de la force expansive de la vapeur de l'eau et de la vapeur de l'alcool, à différentes températures. J. de l'Ecole polytechnique **1**(2), 24–76 (1795)
65. A. Barabell, Improving the resolution performance of eigenstructure-based direction-finding algorithms, in *Proceedings of IEEE International Conference on Acoustics, Speech and Signal Processing (ICASSP)*, vol. 8, 1983, pp. 336–339
66. Y. Hua, T.K. Sarkar, Matrix pencil method for estimating parameters of exponentially damped/undamped sinusoids in noise. IEEE Trans. Acoust. Speech Signal Process. **38**(5), 814–824 (1990)
67. A. Paulraj, R. Roy, T. Kailath, A subspace rotation approach to signal parameter estimation. Proc. IEEE **74**(7), 1044–1046 (1986)
68. Y.C. Eldar, G. Kutyniok, *Compressed Sensing: Theory and Applications* (Cambridge University Press, 2012)
69. R. Alexandru, P.L. Dragotti, Reconstructing classes of non-bandlimited signals from time encoded information. IEEE Trans. Signal Process. **68**, 747–763 (2019)
70. M. Hilton, R. Alexandru, P.L. Dragotti, Time encoding using the hyperbolic secant kernel, in *European Signal Processing Conference (EUSIPCO)* (IEEE, 2021), pp. 2304–2308
71. H. Naaman, S. Mulleti, E. Reznitskiy, N. Glazer, M. Namer, Y.C. Eldar, Sub-Nyquist time-based sampling of FRI signals, in *Show and Tell Demos, IEEE International Conference on Acoustics, Speech and Signal Processing (ICASSP)*, 2021
72. P.E. Debevec, J. Malik, Recovering high dynamic range radiance maps from photographs, in *ACM Siggraph*, 1997
73. K. Yamada, T. Nakano, S. Yamamoto, A vision sensor having an expanded dynamic range for autonomous vehicles. IEEE Trans. Veh. Technol. **47**(1), 332–341 (1998)
74. N.J. Cassidy, Ground penetrating radar data processing, modelling and analysis, in *Ground Penetrating Radar Theory and Applications* (Elsevier Science, 2009), pp. 141–176
75. J. Zhang, J. Hao, X. Zhao, S. Wang, L. Zhao, W. Wang, Z. Yao, Restoration of clipped seismic waveforms using projection onto convex sets method. Nat. Sci. Rep. **6**(1) (2016)
76. Y. Li, M. Safari, R. Henderson, H. Haas, Optical OFDM with single-photon avalanche diode. IEEE Photon. Technol. Lett. **27**(9), 943–946 (2015)
77. T. Olofsson, Deconvolution and model-based restoration of clipped ultrasonic signals. IEEE Trans. Instrum. Meas. **54**(3), 1235–1240 (2005)
78. A. Adler, V. Emiya, M.G. Jafari, M. Elad, R. Gribonval, M.D. Plumbley, Audio inpainting. IEEE Trans. Acoust. Speech Signal Process. **20**(3), 922–932 (2012)
79. Y. Vanderperren, G. Leus, W. Dehaene, An approach for specifying the ADC and AGC requirements for UWB digital receivers, in *IET Seminar on UWB Systems, Technologies and Applications* (IEE, 2006)
80. P. Smaragdis, Dynamic range extension using interleaved gains. IEEE Audio Speech Lang. Process. **17**(5), 966–973 (2009)
81. C. Anderson, S. Venkatesh, J. Ibrahim, R. Buehrer, J. Reed, Analysis and implementation of a time-interleaved ADC array for a software-defined UWB receiver. IEEE Trans. Veh. Technol. **58**(8), 4046–4063 (2009)
82. J. Abel, J. Smith, Restoring a clipped signal, in *IEEE International Conference on Acoustics, Speech and Signal Processing (ICASSP)*, 1991
83. S.-K. Ting, A.H. Sayed, Mitigation of clipping in sensors, in *IEEE International Conference on Acoustics, Speech and Signal Processing (ICASSP)*, 2013
84. B.F. Logan, Signals designed for recovery after clipping–II. Fourier transform theory of recovery. AT&T Bell Lab. Tech. J. **63**(2), 287–306 (1984)
85. A. Janssen, R. Veldhuis, L. Vries, Adaptive interpolation of discrete-time signals that can be modeled as autoregressive processes. IEEE Trans. Acoust. Speech Signal Process. **34**(2), 317–330 (1986)

86. F. Esqueda, S. Bilbao, V. Valimaki, Aliasing reduction in clipped signals. IEEE Trans. Signal Process. **64**(20), 5255–5267 (2016)
87. A. Bhandari, F. Krahmer, On identifiability in unlimited sampling, in *International Conference on Sampling Theory and Applications (SampTA)*, 2019
88. K. Itoh, Analysis of the phase unwrapping algorithm. Appl. Opt. **21**(14), 2470–2470 (1982)
89. A. Bhandari, Unlimited sampling with sparse outliers: experiments with impulsive and jump or reset noise, in *IEEE International Conference on Acoustics, Speech and Signal Processing (ICASSP)*, 2022, pp. 5403–5407
90. D. Florescu, A. Bhandari, Unlimited sampling with local averages, in *IEEE International Conference on Acoustics, Speech and Signal Processing (ICASSP)*, 2022, pp. 5742–5746
91. S. Mulleti, E. Reznitskiy, N. Glazer, M. Namer, Y.C. Eldar, A hardware prototype of sub-Nyquist modulo sampling of FRI signals, in *Show and Tell Demos, IEEE International Conference on Acoustics, Speech and Signal Processing (ICASSP)*, 2021
92. S. Mulleti, E. Azar, S.B. Shah, N. Glazer, S. Savariego, O. Cohen, E. Reznitskiy, M. Namer, Y.C. Eldar, Hardware demonstration of low-rate and high-dynamic range ADC, in *Show and Tell Demos, IEEE International Conference on Acoustics, Speech and Signal Processing (ICASSP)*, 2022
93. R.W. Heath, N. González-Prelcic, S. Rangan, W. Roh, A.M. Sayeed, An overview of signal processing techniques for millimeter wave MIMO systems. IEEE J. Sel. Top. Signal Process. **10**(3), 436–453 (2016)
94. A. Bhandari, R. Raskar, Signal processing for Time-of-Flight imaging sensors: an introduction to inverse problems in computational 3-D imaging. IEEE Signal Process. Mag. **33**(5), 45–58 (2016)
95. Y. Li, C. Tao, G. Seco-Granados, A. Mezghani, A.L. Swindlehurst, L. Liu, Channel estimation and performance analysis of one-bit massive MIMO systems. IEEE Trans. Signal Process. **65**(15), 4075–4089 (2017)
96. J. Choi, J. Mo, R.W. Heath, Near maximum-likelihood detector and channel estimator for uplink multiuser massive MIMO systems with one-bit ADCs IEEE Trans. Commun. **64**(5), 2005–2018 (2016)
97. R.M. Gray, T.G. Stockholm, Dithered quantizers. IEEE Trans. Inf. Theory **39**(3), 805–812 (1993)
98. J. Wolf, J. Ziv, Transmission of noisy information to a noisy receiver with minimum distortion. IEEE Trans. Inf. Theory **16**(4), 406–411 (1970)
99. M.R.D. Rodrigues, N. Deligiannis, L. Lai, Y.C. Eldar, Rate-distortion trade-offs in acquisition of signal parameters, in *Proceedings, IEEE ICASSP*, New Orleans, 2017, pp. 6105–6109
100. K. Yu, Y.D. Zhang, M. Bao, Y.-H. Hu, Z. Wang, DOA estimation from one-bit compressed array data via joint sparse representation. IEEE Signal Process. Lett. **23**(9), 1279–1283 (2016)
101. N. Shlezinger, Y.C. Eldar, Task-based quantization with application to MIMO receivers. Commun. Inf. Syst. **20**(2), 131–162 (2020)
102. P. Li, N. Shlezinger, H. Zhang, B. Wang, Y.C. Eldar, Task-based graph signal compression, https://arxiv.org/pdf/2110.12387.pdf
103. H. Zhang, E. Reznitskiy, N. Shlezinger, N. Glazer, M. Namer, Y.C. Eldar, Task-based low bit quantization for channel estimation, in *Show and Tell Demos, IEEE International Conference on Acoustics, Speech and Signal Processing (ICASSP)*, 2021
104. X. Zhang, H. Zhang, O. Cohen, E. Reznitskiy, S. Savariego, N. Glazer, M. Namer, Y.C. Eldar, Task-based quantization for multi-user signal recovery, in *Show and Tell Demos, IEEE International Conference on Acoustics, Speech and Signal Processing (ICASSP)*, 2022